Compact High Efficiency and Zero-Emission Gas-Fired Power Plant with Oxy-Combustion and Carbon Capture

Paweł Ziółkowski [1,*], Stanisław Głuch [1], Piotr Józef Ziółkowski [2,3] and Janusz Badur [2]

1   Faculty of Mechanical Engineering and Ship Technology, Gdańsk University of Technology, Narutowicza 11/12, 80-233 Gdańsk, Poland; stanislaw.gluch@pg.edu.pl
2   Energy Conversion Department, Institute of Fluid Flow Machinery, Polish Academy of Sciences, Fiszera 14 St., 80-231 Gdańsk, Poland; pjziolkowski@imp.gda.pl (P.J.Z.); janusz.badur@imp.gda.pl (J.B.)
3   Faculty of Civil and Environmental Engineering, Gdańsk University of Technology, Narutowicza 11/12, 80-233 Gdańsk, Poland
*   Correspondence: pawel.ziolkowski1@pg.edu.pl

Abstract: Reduction of greenhouse gases emissions is a key challenge for the power generation industry, requiring the implementation of new designs and methods of electricity generation. This article presents a design solution for a novel thermodynamic cycle with two new devices—namely, a wet combustion chamber and a spray-ejector condenser. In the proposed cycle, high temperature occurs in the combustion chamber because of fuel combustion by pure oxygen. As a consequence of the chemical reaction and open water cooling, a mixture of H_2O and CO_2 is produced. The resulting working medium expands in one turbine that combines the advantages of gas turbines (high turbine inlet temperatures) and steam turbines (full expansion to vacuum). Moreover, the main purpose of the spray-ejector condenser is the simultaneous condensation of water vapour and compression of CO_2 from condensing pressure to about 1 bar. The efficiency of the proposed cycle has been estimated at 37.78%. COM-GAS software has been used for computational flow mechanics simulations. The calculation considers the drop in efficiency due to air separation unit, carbon capture, and spray-ejector condenser processes. The advantage of the proposed cycle is its compactness that can be achieved by replacing the largest equipment in the steam unit. The authors make reference to a steam generator, a conventional steam condenser, and the steam-gas turbine. Instead of classical heat exchanger equipment, the authors propose non-standard devices, such as a wet combustion chamber and spray-ejector condenser.

Keywords: gas-steam turbine; wet combustion chamber; clean gas technology; carbon capture; spray-ejector condenser; zero-emission CO_2 power plant

1. Introduction

The electricity generation sector in Poland is based mainly on hard coal and lignite. Therefore, the diversification of energy sources was the first motivation to create a novel type of thermodynamic gas-fired cycle, which was also to be zero-emission. Another motivation was the requirement to reduce the size of power plants, or combined heat and power plants that would be able to adequately meet the needs of small and medium-sized towns for clean electricity and clean heat. Therefore, there is a requirement for new solutions in terms of clean and compact power plants. In addition, traditional coal- and gas-fired power plants based on conventional technologies are becoming less accepted in the political environment, and especially by environmentalists. Due to the depletion of existing fossil fuel deposits and the growing threat of environmental pollution, society is increasingly interested in innovative and clean technologies related to electricity and heat production. These include carbon blocks equipped with carbon dioxide capture and storage systems (CCS) [1], high-performance combined cycles equipped with CCS systems [2], systems with oxy-combustion [3], systems with biomass gasification or sewage sludge [4,5],

modern hybrid systems with fuel cells [6], geothermal energy transformed into electricity by binary power plant [7], etc. Researchers are working to adapt conventional power plants in such a way as to supply reserve power that could be used in conjunction with unstable renewable energy sources [7].

In this paper, the authors focus on an environmentally friendly and sustainable gas-based solution. Oxy-combustion gas cycles can be applied where shale gas is used at the place of extraction or for gases generated from sewage sludge gasification [8,9]. With this type of fuel, it is becoming increasingly necessary to keep the size of the system reduced, while maintaining high combustion temperatures. It is worth mentioning that biomass and sewage sludge are considered a renewable energy source in Poland, thus there is potential to achieve negative CO_2 emissions [10].

In addition, the effective utilisation of shale gas at the place of extraction in Poland would require compact plants to be built. On the other hand, at sites where biomass or sewage sludge is gasified, it is not always possible to install traditional power supply systems. Therefore, the research outlined in this paper was motivated primarily by the need for energy source diversification and by the search for new power plant solutions, including compact ones. This is why the article opens with an overview of the literature on gas cycles based on oxy-combustion.

1.1. Literature Survey Connected to Oxy-Combustion Thermodynamic Cycles

The following articles [10–12] present a technology that combines gas-steam turbines and clean electricity generation. The paper by Anderson et al. [11] summarises the research on the adaptations made to the GEJ79 turbine. The authors also discuss ways in which to boost steam gas performance in a Siemens SGT900 turbine. An important element of the system is a gas generator into which fuel, pure oxygen, and water, is injected. Then, after burning, a mixture of steam and carbon dioxide is formed, expanding in the turbine. Currently, the first-generation GE J79 turbine is in operation at 11.6 bar pressure and 760 °C. In the second generation, using the SGT900 turbine, there are plans to increase the temperature of a mixture of steam and carbon dioxide before the first stage to 1080–1260 °C. For the third-generation technology, this system will operate at temperatures of 1650–1760 °C and 40 bar [10,11].

Works on the above-mentioned solution are underway in the United States, where, for over 15 years, clean energy systems (CES) have been introducing technologies used in rocket engines for conventional power engineering, thereby building zero-emission power units with power of up to 200:MW [13]. CES cycles have undergone numerous modifications, but the crucial idea is presented in the paper by Hustad et al. [14]. The main elements of the CES cycle are the wet combustion chamber and the expander. The inert medium here is water, not nitrogen. Injected water undergoes phase transition when it receives heat directly from the combustible mixture in the combustion chamber. In CES, the water is injected through a sequential cooling system with appropriately positioned holes. Papers describing the development of the aforementioned solution, both the combustion chamber and the CES cycle itself include [13–17]. Such a concept is fundamentally different from the one described in this article because, water is to be supplied here in the process of thermal transpiration and velocity slip over the entire surface of the combustion chamber [18].

A more complex system to achieve higher efficiencies is the GRAZ cycle in which the working medium is mostly steam [19,20]. Here, the fuel can be both hydrogen and methane.

In the GRAZ cycle, there are several expanders with different purposes. Separation of redundant ingredients (carbon dioxide and excess water) takes place immediately after the condensation of steam from the low-pressure turbine. A high-temperature turbine, on the other hand, operates at much higher temperatures than a high-pressure turbine. This procedure is associated with the introduction of a high-temperature heat exchanger, which acts as a heat recovery steam generator. More information about the operating parameters, as well as proposed dimensions for individual devices in the pilot system, can be found

in [19]. Additionally, it is worth noting that the GRAZ cycle is often analysed as a hydrogen system, both in design states [20], and partial operation regimes [21].

In the cycle with CO_2 recirculation, the carbon dioxide is directed to the combustion chamber instead of H_2O. This statement can be specified with reference to CES and GRAZ cycles, however, with reference to traditional gas turbine cycles, CO_2 operates instead of N_2. These cycles offer great prospects because the structure of the power plant is not as changeable as in CES and GRAZ cycles. As in the well-known gas-steam cycles, there is a clear division between the part where the exhaust gases flow and the steam part where H_2O circulates. The basic difference in the composition of flue gases causes the temperature of the exhaust gases from the gas turbine to rise; therefore, it is possible to change the compression ratios that are achieved in the cycle [2]. Because the cycle is closed, only products that were created in the process of fuel combustion, i.e., CO_2 and H_2O, are released into the environment. Water is recovered in two devices, namely: (1) in the heat exchanger, which is at the same time a flue gas cooler before the compression process, and (2) in the water separator directly before the compressor of the captured CO_2. Extensive analyses of this and other issues related to carbon dioxide capture have been carried out in several publications [22–25]. In the literature [25], these cycles are described as SCO-CC (semi-closed oxy-fuel combustion combined cycle).

The CO_2 prevented emission recuperative advanced turbine energy (COOPERATE) cycle is considered by Yantovski et al. [26] as one of the first emission-free systems. It represents a typical gas cycle in which a split gas turbine with sequential heat supply is used in the following devices: a heat exchanger and two combustion chambers. Of course, in addition to carbon dioxide, fuel and pure oxygen are supplied to it. The other devices of this system are: an oxygen producer, a system of carbon dioxide compressors with intercooling, a water condenser with a separator, and a carbon dioxide condenser with a pump to ensure the increase of the pressure to the parameters required for sequestration and storage. The authors of the cycle estimated the efficiency to be around $\eta = 52\%$ at the turbine inlet temperature (TIT) of 1250 °C [26].

MATIANT is a kind of modification of the COOPERATE cycle in which there is no condensation of carbon dioxide in the condenser designed for this purpose. This is because a proper cooling and compression process maintains supercritical gas parameters [27,28]. Due to the high temperature downstream of the gas turbine, it is possible to transfer the heat flux in the regeneration exchanger to two paths of the working medium. It should also be mentioned that the pressure downstream of the three carbon dioxide compressors is 80 bar. However, the fourth device increase its value to 300 bar. The maximum expected temperature should be 1300 °C and the efficiency of the total cycle $\eta = 45\%$ [27].

Analogously to the MATIANT cycle, the CO_2 loop for energy and nature, enhanced by refrigeration and gas-turbines (COOLENERG) is a modification of the COOPERATE cycle. It is worth noting that this solution includes one combustion chamber and that a significant amount of heat is transferred in the exchanger system [29]. Similar to the two previously mentioned solutions, carbon dioxide as an inert gas, fuel, and oxygen is supplied to the combustion chamber. The main novelty is the added reverse cycle, which provides a source of cooling. Ultimately, this improves the efficiency of the previously considered systems to $\eta = 54\%$.

The zero emissions ion transport membrane oxygen power (ZEITMOP) cycle represents one of the cycles in which CO_2 plays a major role as a working medium. However, due to the ion transport membrane, the ion transport oxygen membrane, and combustion chamber, the authors distinguish three sub-cycles [30], namely: (1) CO_2 sub-cycle, (2) CO_2+H_2O sub-cycle, and (3) air sub-cycle. In the ion transport membrane, a constant temperature of the process has been assumed, which significantly affects the transport of ions on both the air and CO_2 sides. This assumption also determines the temperature at the nodal point at the beginning of the process in the next device. Cycle efficiency was estimated in the range of $\eta = 46–56\%$ for TIT = 1300–1500 °C [30], respectively.

The paper by Park et al. [31] presents a proposal for a system of combined solid oxide fuel cell (SOFC) with the use of oxy-combustion. The presented fuel cell does not differ in the main working principle. Similar to the case of hybrid systems [32,33], the air—pre-compressed in a compressor and properly preheated in a series of exchangers—flows into the cathode. Then, some of the air goes to the ion membrane of the oxygen transport to obtain pure oxygen for the oxy-combustion in the combustion chamber. From the anode side, a mass flow rate of the fuel, which did not react in the cold combustion process, is extracted. It should be added that the fuel (for example, methane) should be reformed so that H_2 and CO receive the reaction surface of the anode. Ultimately, unburned fuel, pure oxygen, and water, which is the inert medium, will end up in the combustion chamber. The medium created in this way performs two functions—namely, it first heats the air flowing into the gas turbine and then expands in an expander. It should be mentioned that similar analyses were conducted in the papers [34,35], but without using the ion transport membrane. Kvamsdal et al. obtained the highest efficiencies of a fuel cell system with a gas turbine out of nine considered solutions featuring carbon dioxide capture [35]. In other solutions, fuel is reformed before the fuel cell to which oxygen is then supplied [32,36].

The paper [37] presents design and computational fluid dynamics analysis of the last stage of an innovative gas-steam turbine. The authors investigated blades operating under the same conditions identical to those discussed in the paper. It was found that the geometry of the last stage for gas-steam turbine resembles that of the steam turbine, but in-flow condensation does not occur, because the fluid temperature is higher than would be the case in the conventional steam cycle. Droplet erosion problems are eliminated.

1.2. Elements of Compact Steam-Gas Power Plant with Oxy-Combustion and Carbon Capture

Oxy-combustion as a CO_2 capture technique leads to a reduction in the size of both boilers and gas turbines. This is because it provides for the conversion of chemical energy with more control over the contribution of a given inert medium. Of course, there is still the problem of proper cooling of the combustion chamber walls and stages of the gas turbine, but this can be solved by techniques with transpiration-type cooling [18,37]. So far, two solutions for the introduction of oxy-combustion technology have been developed: the first one with a predominance of steam, and the second one with a predominance of CO_2. Most of the publications on oxy-combustion in gas turbines concern the replacement of nitrogen with carbon dioxide [22–31,38]. However, installations and solutions in which steam is the main working medium have a greater potential to reduce size. They are based on hydrogen fired turbines and gas turbines with steam or water injection.

In the literature, experimental works with the application of oxy-combustion are becoming more important [39–42]. For example, Saanum and Ditaranto in the article [43] have evolved an innovative burner in which CO_2 is an inert medium. Applied pressure and temperature in above mentioned research are similar to those in gas turbines. Researchers also conduct a theoretical work aimed not only at the efficiency of the whole plant, but also at the heat and mass transfer processes in the burner area itself. There is a growing interest among researchers who model these processes using computational fluid dynamics (CFD) [44–49]. Moderate or intense low oxygen dilution (MILD) techniques are developing to maintain low levels of nitrogen oxide production [50]. Moderate and intensive low-oxygen dilution oxyfuel combustion technologies, in which the advantages of oxy-combustion and MILD technology are combined, are also intensively developed [51,52].

Contrary to pre-combustion systems [53,54] requiring huge gasification installations, or post-combustion technologies [55–59], in which it is necessary to add an additional island of equipment behind the boiler or gas turbine in the oxy-combustion plant, authors aspire to reduce the size of power units. An additional element here is the air separation unit (ASU) or carbon capture unit (CCU). However, it is important to point out that oxygen can be produced in a different place.

The process of obtaining O_2 is easily separable from the rest of the installation. The ASU station will be described in the Section 2. The concept of producing O_2 is adapted to the needs of the cycle presented in this article.

In addition to the reduction of carbon dioxide in the case of oxy-combustion, it is possible to obtain lower emissions of nitrogen oxides compared to traditional methods of NOx reduction. Primary and secondary reduction techniques have been developed in gas turbines. A well-known and well-established solution is the use of dry low emission burners (DLE) [59,60]. Other methods of primary NOx emission reduction are, for example, steam injection into the combustion chamber, as demonstrated by the Cheng cycle, or water injection—wet low emission (WLE) technology [61,62]. Secondary technologies of reducing the nitrogen oxides emission in exhaust gas are selective catalytic reduction (SCR) and selective non-catalytic reduction (SNCR) [63]. However, the above-mentioned methods require an extensive system of equipment which affects the system size and efficiency. Oxy-combustion eliminates nitrogen from the substrates that means the contribution of reactions, where nitrogen oxides would be formed, is negligible. Additionally, it is much easier to reduce the size of the whole unit, in contrast to secondary and primary combustion in the burning process without nitrogen.

Due to the possibility of obtaining much higher temperatures in the combustion chamber there is a significant opportunity for the degradation of various types of ingredients appearing in alternative fuels. They come from shale gas deposits or sewage sludge gasification. The cycle proposed in this article is dedicated to such fuels gained in specific conditions. Energy from waste is also increasingly mentioned [64]. This solution is to ensure the compactness of the cycle and the burning of all fuel components in a high-temperature combustion chamber.

Natural gas exploited by traditional methods is commonly considered a conventional gaseous fuel. On the other hand, shale gas production has started due to horizontal drilling and fracturing. These deposits are characterized by relatively rapid depletion. Therefore, it is not always profitable to build a conventional power plant or to transmit gas on the scale as it is in the North America. Therefore, for a short period of production, it became purposeful to design compact dedicated equipment.

According to the referenced papers [65,66], the prices—and, thus, the exploitation—of shale gas do not correspond to the prices of conventional gas, which is connected to market uncertainty and investors' concerns. The most important factor influencing shale gas production is its economic viability, which, in turn, in Polish economic conditions, is dictated by the prices of natural gas supplied from other countries. However, it should be noted that despite the profitability of unconventional gas production in the U.S. and Canada [67–69], shale gas deposits in Poland are approximately three times deeper; therefore, the cost of production is estimated to be at least three times higher [66]. Thus, it is unlikely that this cycle will be used for burning shale gas on Polish soil.

Another future application of this system is wastewater treatment plants, where the resulting sludge can be gasified. Then, the gas burned at a high temperature is produced through oxy-firing. Sludge is a wastewater treatment residue that is biologically active and consists of water and organic matter as well as organic and inorganic pollutants, such as polycyclic aromatic hydrocarbons (PAHs) and heavy metals. Disposal methods, leading to stabilisation and safe recycling, are gradually replacing landfilling, storage, and spreading on the ground. In EU countries, new methods are becoming more popular, for both environmental and economic reasons, as landfilling is considered to be the most expensive method of sewage sludge disposal [70–72]. One such method may be the combination of a sewage sludge gasifier with the cycle proposed in this article.

Currently, in Poland, there are at least 45 installations for drying sewage sludge and 12 installations using solar energy. Combustion can take place in existing combustion units (at least 11), which are based on fluidised bed (mainly) and scaffold furnaces. In addition, combustion is possible in 13 cement producing facilities in Poland, as well as in existing or advanced construction (near commissioning) of municipal waste incinerators in 17 cities.

In all these cases, logistics is of decisive importance for the economic feasibility of the solution. Therefore, the problem of sewage sludge is most serious in the case of small and medium-sized towns without their own thermal treatment plant, with limited possibilities for local land use [72]. In the case of gases from the sewage sludge gasification process, chlorine compounds will likely be found and should be burned at the highest possible temperature. For the above reasons, oxidation may prove to be more beneficial than other carbon capture and reduction techniques. Other types of waste can also be burned, but this must be carried out under appropriate conditions [64]. Therefore, it is reasonable to look for new solutions for the disposal of this type of waste.

1.3. Purpose and Scope of the Article

The main aim of this article is to present a thermodynamic analysis of the oxy-combustion cycle, which uses two new devices. The first progress towards such a solution was achieved in Ziółkowski's works [3,7], and a summary was included in his dissertation [9]. Some of the results are available in subsequent publications, which present an analysis of the successive thermodynamic cycles [8,73,74]. Starting from well-known traditional gas cycles with regeneration [73], through combined cycles with steam injection [74], a system based on a double Brayton cycle with oxy-combustion and CO_2 capture (DBCOCC) has emerged. Innovative systems also include a compact, highly efficient, emission-free power plant cycle, here called DBCOCC, in which water is supplied through the walls of the combustion chamber.

A brief discussion of the new cycle in a compact, high-efficiency, emission-free power plant can be found in Section 2. The aforementioned section also applies to the oxygen production station (air separation unit) and the sub-cycle of the spray-ejector condenser. Mass, momentum, and energy balance equations and characteristic parameters of the spray-ejector condenser are defined in Section 3. The results of thermodynamic calculations are discussed in Section 4. Section 5 provides an example of minimising the dimensions of a steam generator and a condenser. A brief summary of the new purpose of the proposed cycle is presented in the conclusions and perspectives (Section 6).

2. Thermodynamic Cycle of a Compact, High-Efficiency, Zero-Emission Power Plant

Figure 1 shows a schematic diagram of the thermal cycle of a gas-steam turbine combining the idea of oxy-combustion with the use of water injection into the combustion chamber. The characteristic points of the cycle corresponding to the relevant processes in the T–s diagram are indicated on it (Figure 2). First, the compression of oxygen produced in the air separation unit is shown (CO_2 points 1–2). It goes to a wet combustion chamber, where stoichiometric combustion of methane occurs. The mixture produced in this way is cooled with water, which is transformed into steam. Another important process of this solution is the expansion of the working medium in a high-temperature gas turbine (GT points 3–4 in Figures 1 and 2), followed by the expansion of the flue gas in conditions below atmospheric pressure (GT^{bap} points 4–1^{bap}).
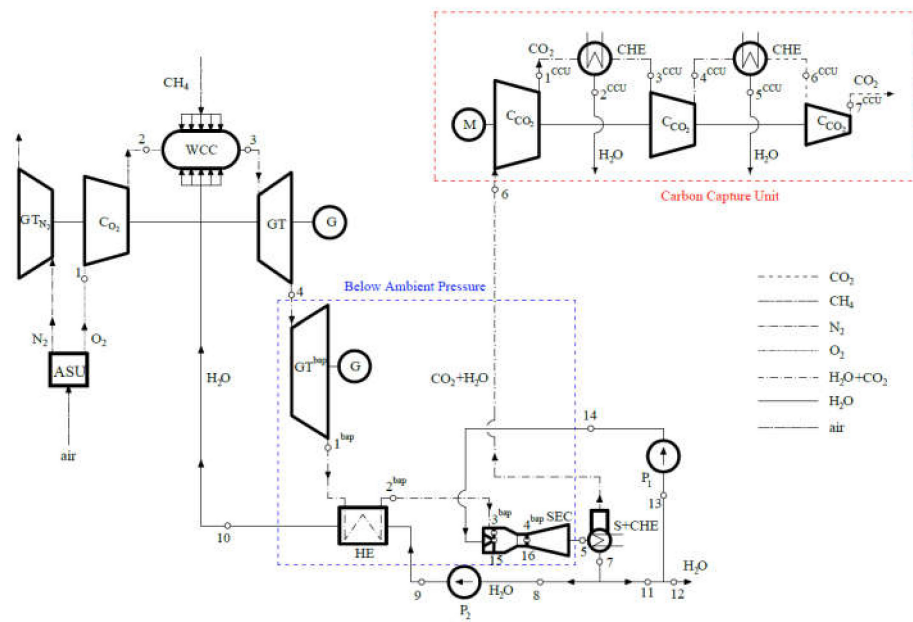
Figure 1. The double Brayton cycle with oxy-combustion and CO_2 capture (DBCOCC), where WCC—wet combustion chamber, GT + GT^{bap}—gas turbine divided into two parts, SEC—spray-ejector condenser, ASU—air separation unit, C—compressor, HE—heat exchanger, CHE + S—condensate-cooler heat exchanger and separator, CHE—cooling heat exchanger, M—motor, G—generator, P_1—supply water pump, P_2—water pump for cooling combustion chamber, GT_{N2}—expander N_2, C_{CO_2}—CO_2 compressor.

Figure 2. T–s diagram of the DBCOCC cycle.

The regeneration exchanger (HE) then heats the water (points 9–10) and cools the exhaust gas (1^{bap}–2^{bap}). The mass flow rate of flue gases, after the transfer of thermal energy, goes to the spray-ejector condenser, where it is compressed to the state specified in point 5. However, the water driving the nozzle and the flue gases sucked in from point 2^{bap} are on a single line, with a cross-section of $3^{b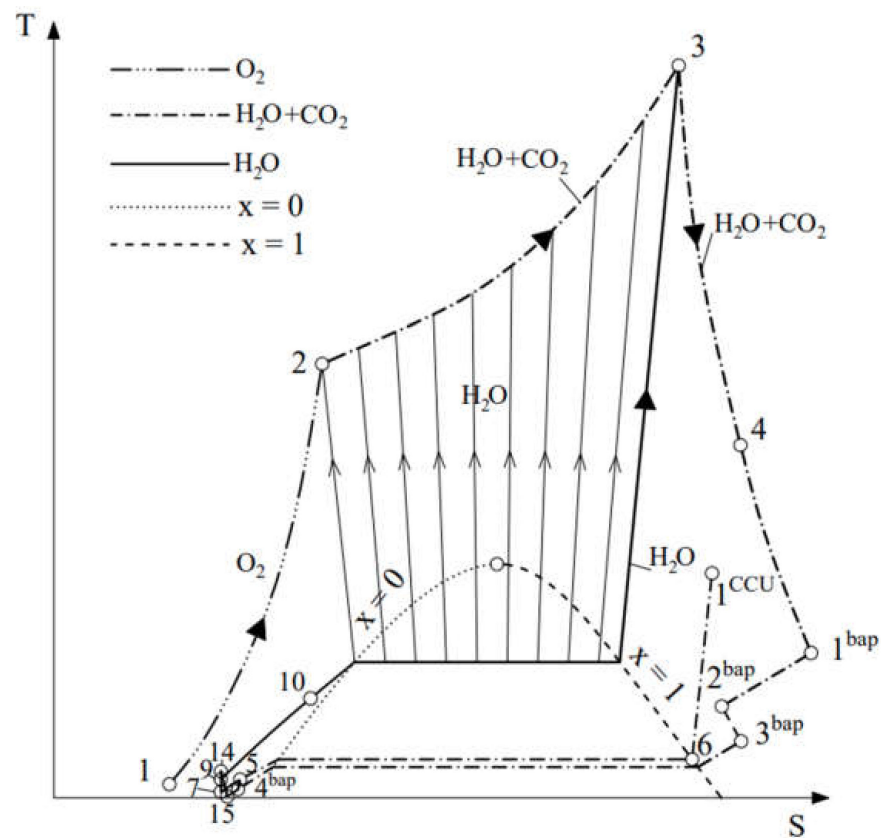ap}$–15. The cooling and compressing water and the condensed flue gases are mixed between points 3^{bap} and 4^{bap} (or 15 and 16). Adequate heat transfer surface can be provided by millions of drops injected through the shaped spray nozzle.

It can be assumed that the complete mixing of the medium has already taken place in point 4^{bap}, the thermodynamic parameters of which become the same as in point 16. In a spray ejector condenser (SEC), the water vapour and flue gases first expand and then mix together. Finally, in the diffuser, the pressure is increased to about 1 bar (point 5). The purpose of the applied modification is to reduce the dimensions of the condenser compared to a solution without water injection on the working medium flowing out of the turbine. On the other hand, a similar heat transfer surface area as in classical condensers is achieved by a huge value of volumetric surface density [75].

Another device is a heat exchanger joined with a separator in which the resulting mixture is cooled, and carbon dioxide and part of the steam are separated from water (S+CHE). Clean and cooled water flows out at point 7 and is then directed to two pumps—namely, low-pressure P_1 and high-pressure P_2. Some of the water produced during combustion condensates into the SEC; thus, a certain excess of the working medium has been created, which is removed from the cycle in point 12. The P_2 pump, on the other hand, ensures that the pressure is increased to 40 bar and that water is directed to cooling the combustion chamber.

The last process occurring in DBCOCC is carbon capture, which takes place in a series of devices (carbon capture unit). Starting from point 6, the mixture of carbon dioxide and steam is compressed and the water is gradually condensed in subsequent exchangers (CHE). As can be seen in the next set of devices (C_{CO_2}+CHE), the CO_2 pressure increases and the water content decreases. The final result is pure carbon dioxide at 80 bar at point 7^{CCU}.

It is also worth noting that a mixture of steam and carbon dioxide is generated in a wet combustion chamber, which then expands in the turbine. For such a medium, the adaptation of a gas turbine due to temperatures and the adaptation of a steam turbine due to its size in the low-pressure part may be considered. However, in this situation, it is most justified to design a brand-new expander that will combine the advantages of both devices. An important element of the system is the air separation unit (ASU), which is described in the next section.

2.1. The Mechanism of ASU

There are several basic methods for separating O_2 from other air components—namely, absorption, adsorption, cryogenic methods, membrane methods, and chemical loop-based methods [76–78]. It should be mentioned that, depending on the method, there are different levels of development, ranging from proven ones, such as cryogenic, adsorption, and membrane methods using polymers, to technologies developed in scientific laboratories, using ionic membranes [79].

This thermodynamic analysis is based on the cryogenic method, which is the most developed and currently the only one suitable to produce oxygen in sufficient quantities for use in a gas and steam turbine [76–82]. Based on the articles [78,79], it was found that the performance of this method is at least an order of magnitude higher than that of other methods, including adsorption. The cryogenic air separation method is based on the distillation of gases in at least two columns with different pressures. This is the most mature technology and provides a high oxygen purity of 95–99.8%. Separating argon as a separate fraction increases the purity of both oxygen and nitrogen. Cryogenic methods can also be used to separate CO_2 from the flue gases.

In this article, separation in the case of cryogenic methods is based on the use of several devices employing an equilibrium of phases in given thermodynamic parameters. Therefore, there are compressors, heat exchangers, and rectification columns in the system that act as separators. Figure 3 shows a scheme of the system used to produce oxygen. Because air consists mainly of cryogenic gases, the commonly known Linde columns are used for air separation. It should also be mentioned that the introduction of oxy-combustion with the use of these columns causes the loss of efficiency of the power plant, which typically oscillates at the level of 7–8.8%.
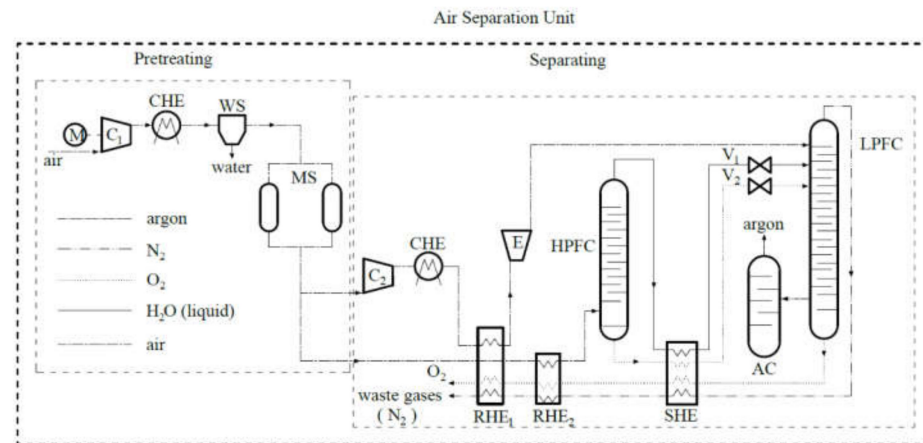

Figure 3. Air separation unit (ASU), where C—compressor, M—motor, RHE—regenerative heat exchanger, CHE—cooler, SHE—subcooler, E—expander, WS—water separator, MS—molecular sieve, V—valves, AG—argon column, LPFC and HPFC—low-pressure fractionating column and high-pressure fractionating column [76].

However, there are also other types of installations, such as those transferring heat for the evaporation of LNG [83,84], with binary engines [85] and with O_2 storage tanks to improve the efficiency of ASU [86]. Additionally, new methods of analysis are being developed, which combine balances to improve the cyclic operation efficiency and thus reduce the energy consumption of ASU stations and other devices supporting or utilizing heat and waste operation [87–89]. An air separation unit (ASU) including Linde columns is shown in Figure 3. Its individual elements were modelled in relation to the work of [76]. The main ASU devices include:

- main compressor (C1);
- pre-cooling heat exchanger (CHE);
- cleaning by molecular sieve (MS) and compressed air drying in water separator (WS) systems;
- second compressor (C2), a cooler (CHE), and an expander (E);
- high-pressure (HPFC) and low-pressure (LPFC) fractionating columns;
- exchangers, namely, regenerative heat exchanger (RHE1, RHE2); subcooler (SHE);
- valves (V1, V2).

In the liquefaction process, Linde used the phenomenon of isenthalpic throttling (Joule–Thomson effect) of pre-cooled air in the regenerative heat exchanger (RHE).

As stated in [42], the largest cryogenic oxygen generating station produces 4200 tonnes of oxygen per day using a compressor with a capacity of 700,000 m^3/h and 50 MWe.

Further development of these methods is expected due to the concept of introducing hybrid systems in combination with membrane methods [76].

An important feature of cryogenic methods is that, by slightly reducing air purity, the energy consumption of the process is significantly reduced. This relationship corresponds to a situation in which, at 99% air purity, 100 units of energy should be supplied, and changes in the range from about 95 to 99.9% are described by an exponential curve. Therefore, this
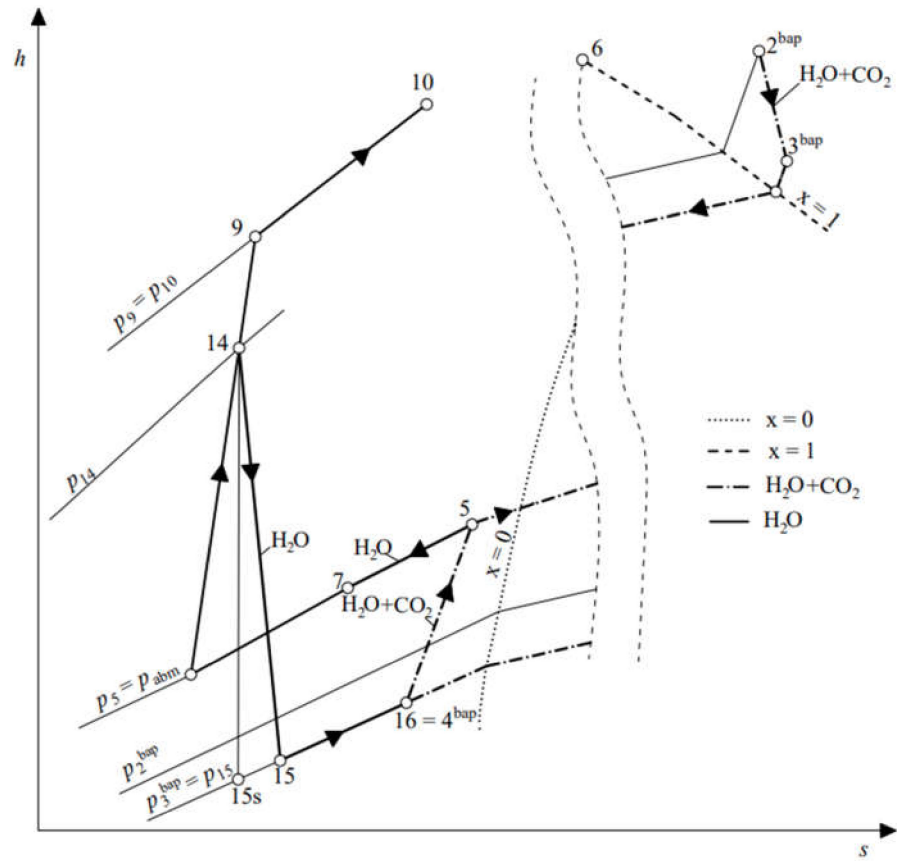
article assumes that the oxygen purity will be at a level of 98.9%, which is sufficient for an oxy-combustion power plant.

2.2. Sub-Cycle of the Spray-Ejector Condenser

It is worthwhile to more thoroughly examine the sub-cycle of the spray-ejector condenser. It is closely related to the surrounding area below the ambient pressure, as can be seen in Figure 1. Its zoom, together with the indicating of key nodal points, is shown in Figure 4. In the wet combustion chamber (WCC), an unusual working medium is formed, consisting of 80–90% steam and 10–20% CO_2. It is therefore important to separate the steam from the CO_2 accordingly. The working fluid expands in a gas-steam turbine that is divided into two parts—namely, GT+GT^{bap}. In the high-temperature turbine (GT), the expander operates at pressures above atmospheric pressure. The second part (GT^{bap}), which corresponds to the low-pressure steam turbine, works below ambient pressure. The original idea, around which this article concentrates, is also the introduction of an ejector that acts as a spray-ejector condenser (SEC). The sub-cycle of the SEC is closed by a P_1 pump, which feeds the water driving the ejector.

Figure 4. A schematic diagram with the precise location of the most important junction points of the cold sub-cycle, where GT^{bap}—gas turbine operating at negative pressure, SEC—spray-ejector condenser, HE—regenerative heat exchanger, G—generator, P_1—supply water pump, P_2—recirculation pump, S+CHE—separator and condensate cooling heat exchanger.

The very idea of using a spray-ejector condenser is not new. Thus far, the idea of water injection into the condensers has been implemented in steam-powered cargo ships as a compact water condenser. In power plants, on the other hand, a similar device is used to maintain the vacuum in the condensers for air extraction and is commonly called a water ejector. It sucks the air and steam from the condenser and is therefore part of the vacuum maintenance system. This is particularly important not only for traditional power plants but now also for the compact DBCOCC system. This is shown in the graphs *h–s*, *T–s*, and *p–h* (Figure 5,Figure 6,Figure 7).

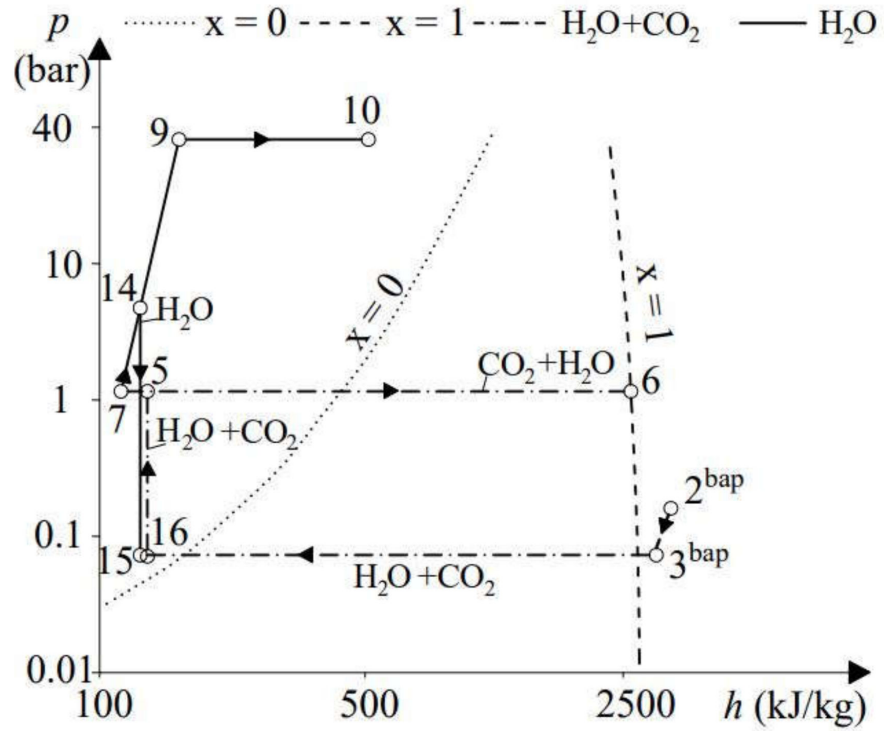**Figure 5.** *h–s* diagram of the SEC sub-cycle.
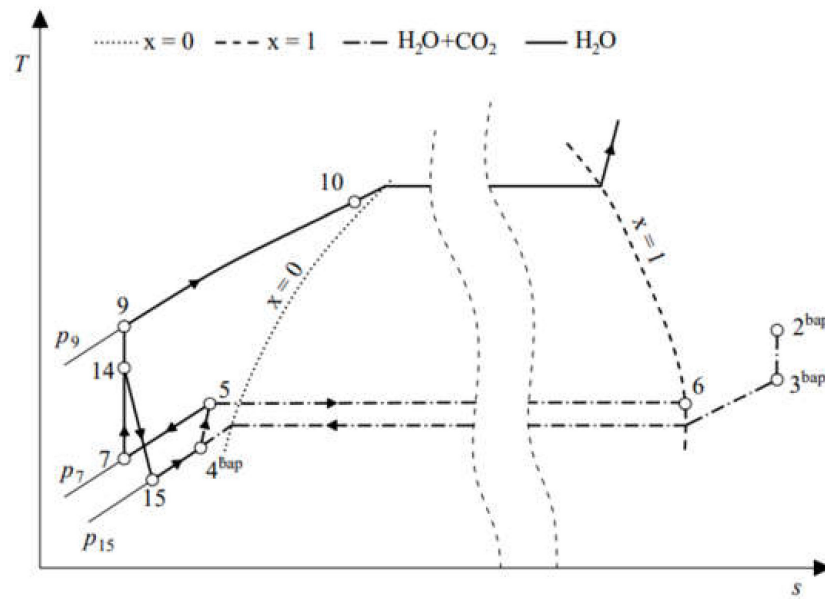
Figure 6. *p–h* diagram of the SEC sub-cycle.

Figure 7. T–s diagram of the SEC sub-cycle.

The condensation process parameters directly affect the efficiency of the power plant by maintaining an adequate vacuum behind the last stages of the turbine. The condensing temperature in classical condensers depends on the saturation pressure and is one of the most important parameters of the thermodynamic cycle [90]. Basically, a spray-ejector condenser consists of a liquid-gas ejector located at the outlet of a vacuum turbine. The next device is a carbon dioxide separator and a water cooler marked as S+CHE in Figure 4. A detailed scheme of the liquid-gas ejector with the marking of characteristic areas is shown in Figure 8. The elements of the ejector are as follows: primary nozzle (power supply nozzle), suction chamber (supply chamber), secondary nozzle (delivery nozzle) with mixing chamber, and diffuser. The characteristic working cross-sections are:
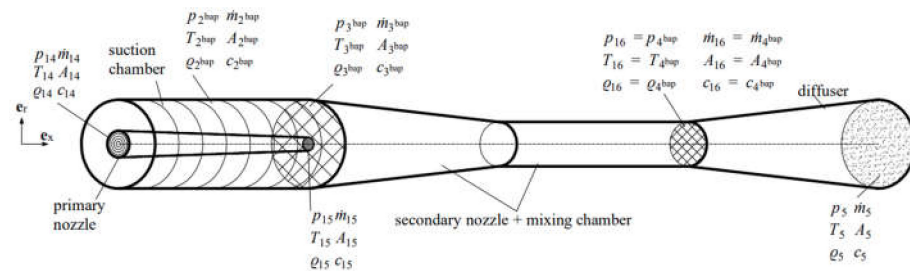

Figure 8. SEC with characteristic parameters included in mass, momentum, and energy equations.

The inlet cross-section of the primary nozzle with a characteristic cross-sectional area A_{14};

The outlet cross-section of the primary nozzle with a characteristic cross-sectional area A_{15};

The inlet cross-section of the suction chamber with a characteristic cross-sectional area $A_{2^{bap}}$

The outlet cross-section of the suction chamber with a cross-sectional area $A_{3^{bap}}$;

The mixing chamber with a characteristic cross-section $A_{16} = A_{4^{bap}}$; and

The outlet cross-section of the diffuser with a characteristic cross-sectional area A_5.

In this article, the SEC is a device that, in addition to maintaining a sufficient level of vacuum, will ensure the compactness of the structure. This reduction in size is made possible by shortening the vapour condensation path, which does not need to flow over a dozen rows of tubes to cool down and then condense [91]. Due to direct mixing with cooling

water, immediate volumetric condensation appears. This can be seen in the diagrams *h–s*, *T–s*, and *p–h* (Figures 5–7).

In Figure 5, the following thermodynamic processes can be distinguished: 14–15—acceleration of the working medium in the primary nozzle; 14–15$_s$—ideal process of accelerating the working medium; 2^{bap}–3^{bap}—suction of the medium into the suction chamber; 15–16 and 3^{bap}–4^{bap}—exchange of mass, momentum, and energy in the mixing chamber; and 16–5 (or 4^{bap}–5)—compression of the working medium in the diffuser. Additionally, processes occurring in pumps can be identified, i.e., in P$_1$ (7–14) and P$_2$ (7–9), in the regeneration exchanger (points 9–10), and separation in S+CHE (thermodynamic processes 5–6 and 5–7).

The condition for the operation of the liquid-gas ejector requires a lower pressure region ($p_{3^{bap}} = p_{15}$) at the outlet of the primary nozzle (point 15) than in the cross-section $A_{2^{bap}}$.

The lower the pressure p_{15}, but also lower than the suction section pressure $p_{2^{bap}}$, the more effectively the mass flow rate of the working mixture will be sucked in. However, as a result of the phase transition of steam into water, the resulting vacuum contributes to improving the conditions for maintaining a vacuum. The mass flow rate of the sucked mixture $\dot{m}_{2^{bap}}$ possesses much less kinetic energy compared to the kinetic energy of the mass flow rate of water $\dot{m}_{14}$. Therefore, a mass flow rate at the outlet of the diffuser $\dot{m}_5$ has a significant amount of kinetic energy supplied by the $\dot{m}_{14}$ and only a limited part of it is converted into suction and compression work [92–94]. This process of energy conversion in the liquid-gas ejector strongly depends on the nozzle design.

There must be a total pressure difference between the inlet (point 14) and outlet (point 5) for the flow as a whole to occur in a specific direction; $p_{14} > p_5$. Therefore, the flow channel of the ejector must be shaped in such a way that the pressure drop $p_{14} - p_5$ will not be linear and that, in addition, it will reach its minimum for $p_{3^{bap}} = p_{15}$. Thus, the pressure drop $p_{14} - p_5$ will be far from the uniform linear drop, and the pressure changes themselves are shown in Figure 6. The diagram shows the region of strongly reduced pressure $p_{3^{bap}} = p_{15}$ such that $p_{3^{bap}} < p_{2^{bap}}$.

As a result of a specially shaped primary nozzle, the kinetic energy of the water mass flow rate with pressure p_{15} sucks gas from the area with higher pressure $p_{2^{bap}} > p_{15}$ to the lower pressure area $p_{3^{bap}} = p_{15}$. In a properly operating ejector, there is a relationship between the pressures in individual sections: $p_{15} \leq p_{2^{bap}} \leq p_5 \leq p_{14}$. In practice, there appear to be high-pressure liquid-gas ejectors $\pi_{cs} = \frac{p_5}{p_{15}} > 30$. However, the pressure ratio for ejection and suction ($\pi_{ns} = \frac{p_{14}}{p_{15}}$) can range from 10 to 100 [92–94].

The area of phase transition is highlighted in the Figures 5–7, where *x* = 0 is a saturated liquid and *x* = 1 is a saturated vapour. Additionally, in the *T–s* diagram (Figure 7), there is a zoom of Figure 2, but it concerns the area associated with the phase transition and the operation of the spray-ejector condenser (SEC).

2.3. COM-GAS Code

Computational flow mechanics (CFM) methods are used for simulations, which are based on integral (algebraic in space) equations of mass, momentum, and energy balance. For example, in CFM, at the engineering level (0D) treat a device as a "black box" that has inlets and outlets, heated surfaces on which heat is exchanged, and a moving surface (blades) on which energy is converted to the purpose of work. It is necessary to use zero-dimensional modelling (0D) that relates to the design level strictly focused on thermodynamic parameters at specific points in the thermodynamic cycle.

In Section 2, the mathematical model of the proposed, compact high efficiency and zero-emission power plant with oxy-combustion and carbon capture cycle and its implementation in an in-house code termed COM-GAS is presented. This software allows the prediction of basic parameters, such as temperatures, combustion composition, efficiency, and other related factors. A detailed description of the COM-GAS programe and the procedures it contains can be found in papers [6–8,33].

3. Governing Equations

Figure 4 shows the most important elements of the construction of a liquid-gas ejector as a spray-ejector condenser with a water-carbon dioxide separator. Preceding works presented the model of this device [3,8]. In the following subsections, integral parameters will be defined, describing the characteristics of the liquid-gas ejector, phenomenological models of the mixing process, and basic mass, momentum, and energy balances. The closures will also be presented, which should be obtained from dedicated experiments, or extracted from the literature on the issue. Definitions of power and efficiency will conclude the section devoted to governing equations.

3.1. Integral Parameters

The main characteristic of the operation of the liquid-gas ejector is the dependence of the dimensionless compression ratio (Π) on the volumetric entrainment ratio (χ). The mass entrainment ratio can be distinguished in the literature:

$$\chi_m = \frac{\dot{m}_{2^{bap}}}{\dot{m}_{14}} \tag{1}$$

where there is a relatively large disproportion between the motive ($\dot{m}_{14}$) and the suction mass flow rate ($\dot{m}_{2^{bap}}$)—namely, at the level of 10^{-3}. Due to such a large disproportion between the motive mass flow rate ($\dot{m}_{14}$) and the suction mass flow rate ($\dot{m}_{2^{bap}}$), a volumetric entrainment ratio (χ) defined as follows is also used:

$$\chi = \frac{\dot{V}_{2^{bap}}}{\dot{V}_{14}} \tag{2}$$

where $\dot{V}$ is the volume flow rate. χ extends over a wide range—namely, $\sim 10^{-1} - 7$.

The next parameter is the energy efficiency of the liquid-gas ejector, expressed by:

$$\eta = \frac{N_{Ce}}{\dot{E}_e} \tag{3}$$

where there is a compression power P_{Ce}, and the available energy rate which is supplied by primary nozzle $\dot{E}_{14}$. Referring to the parameters shown in Figures 4–7, the compression power is as follows:

$$P_{Ce} = (\dot{m}_{2^{bap}} + \dot{m}_{14})(h_5 - h_{16}) \tag{4}$$

where h_{16} is the specific enthalpy in the inlet cross-section of the diffuser and h_5 is the specific enthalpy in the outlet cross-section of the diffuser.

In turn, the available energy rate that is supplied by the primary nozzle is presented as:

$$\dot{E}_{14} = \dot{m}_{14} \left(u_{14} + \frac{p_{14}}{\rho_{14}} + z_{14}g + \frac{1}{2}c_{14}^2 \right) \tag{5}$$

where u_{14}—specific internal energy; p_{14}—static pressure in the inlet cross-section of the primary nozzle; ρ_{14}—density in the inlet cross-section of the primary nozzle; z_{14}—height in the inlet cross-section of the primary nozzle; and c_{14}—velocity at the inlet cross-section of the primary nozzle. In the literature, there is also a definition referring to the work done on the sucked gas itself:

$$\eta_{SEC} = \frac{P_{Cs}}{\dot{E}_{14}} \tag{6}$$

where there is also work consumed by the compressed gas and steam that changes into water:

$$P_{Cs} = \dot{m}_{sg(16)}w_{16,5g} + \dot{m}_{H_2O(lq)}w_{16,5} \tag{7}$$

where $w_{16,5g}$ is the specific work of non-condensed gases to compress to pressure at the outlet of the diffuser (points $16 - 5$); $w_{16,5}$ is the specific work of condensed steam to compress to pressure at the outlet of the diffuser (points $16 - 5$); and $\dot{m}_{H_2O(lq)}$ represents condensed water due to phase transition and $\dot{m}_{sg(16)} = \dot{m}_{2^{bap}} - \dot{m}_{H_2O(lq)}$. Equation (6) is close to the definition of compressor efficiency in which the work of sucked gas, in the form of the kinetic energy of the movable walls, converts in the outlet diffuser into the compression.

If dimensionless parameters related to pressure are taken into consideration the following equations should be considered [94,95]:

- pressure ratio with regard to suction pressure:

$$\pi_{ns} = \frac{p_{14}}{p_{2^{bap}}} \tag{8}$$

- pressure ratio with regard to pressure at the outlet from the spray-ejector condenser:

$$\pi_{sc} = \frac{p_5}{p_{2^{bap}}} : \tag{9}$$

where pressures ($p_{2^{bap}}$; p_5; p_{14}) are presented in Figure 8. Pressure ratios are correlated with the measurements $\pi_{ns} > \pi_{nc}$. A more complex definition is characterised by coefficients taking into account the differential pressure, namely:

- the dimensionless suction ratio:

$$\Pi_s = \frac{p_5 - p_{2^{bap}}}{p_{14} - p_{2^{bap}}} = \frac{\pi_{cs} - 1}{\pi_{ns} - 1} \tag{10}$$

- the dimensionless compression ratio:

$$\Pi_c = \frac{p_5 - p_{2^{bap}}}{p_{14} - p_5} \tag{11}$$

- the dimensionless cavitation ratio:

$$\Pi_{cav} = \frac{p_{14}^t - p_{sat}(T_{14})}{p_{2^{bap}}^t - p_{sat}(T_{14})} \tag{12}$$

where $p_{sat}(T_{14})$—the saturation pressure of the liquid at a given temperature; $p_{14}^t = p_{14} + \rho_{14}\frac{c_{14}^2}{2}$—total pressure at the inlet to the ejector; and $p_{2^{bap}}^t \approx p_{2^{bap}}$—total pressure in the suction area assuming that the velocity at the inlet to the suction chamber $c_{2^{bap}} \approx 0$.

These basic values are calculated using direct measurements. The basic curves used to determine the type of ejector are [93,94]:

- the dimensionless suction ratio as a function of the entrainment ratio: $\Pi_s = \Pi_s(\chi)$
- the dimensionless compression ratio as a function of the entrainment ratio: $\Pi_c = \Pi_c(\chi)$
- the dimensionless cavitation ratio as a function of the entrainment ratio: $\Pi_{cav} = \Pi_{cav}(\chi)$
- the efficiency characteristics: $\eta = \eta(\chi)$

The utility of integral characteristic is based on their experimental designation [93,94]. At present, however, certain principles design the geometry of the ejector to provide sufficient performance [95–97]. In the current state of the development of numerical modelling, the calibration of models is becoming crucial with regard to experimental characteristics [97–103]. Therefore, it can be concluded that the development of CFD modelling allows for the obtaining of characteristics that could be compared to the measurement at the level of 20%. However, to describe the basics of both 3D and 0D models, it is necessary to present the basics of classical phenomenological models that are derived from experimental mea-

surements [100–103]. For such an unusual device as a spray-ejector condenser, a dedicated experiment should be prepared.

3.2. Mixing and Condensation Process for the Spray-Ejector Condenser

In general, the mixing process of the components combined with the condensation of one of them involves the simultaneous transfer of mass, momentum, and energy between the two flows. However, even in a particularly simple case in which mixing flows have the same temperature and pressure, the mixing process in the flow is extremely complex. Due to the specifics of geometry and parameters, it has become common within the literature to distinguish three different mechanisms that determine whether the ejector works like a compressor, even in the case of isothermal mixing. These are the mechanisms discovered by classical experimentation:

Witte shock mixing [104,105];

Darcy–Weisbach friction mixing [100,106]; and

Flügel–Cunningham pulse mixing [107,108].

These mechanisms are fully three-dimensional, especially when the asymmetry of the suction chamber of the spray-ejector condenser is considered. The equation describing all forces provided by the mixing fluids is recorded in the form of one vector as:

$$F = \iint\limits_{\partial V} \left(p\mathbf{I} + \boldsymbol{\tau} + \mathcal{R} + \mathbf{f}_{\partial V} \bigotimes \mathbf{n} + \mathbf{n} \bigotimes \mathbf{f}_{\partial V} + \mathbf{D} + \mathbf{P} \right) \mathbf{n} \, dA \qquad (13)$$

where p—pressure, $\mathbf{I}$—unit tensor, $\boldsymbol{\tau}$—viscous stress tensor, $\mathcal{R}$—Reynolds stress tensor, $\mathbf{f}_{\partial V} \otimes \mathbf{n} + \mathbf{n} \otimes \mathbf{f}_{\partial V}$—the tensor resulting from the forces of mobility, $\mathbf{n}$ normal vector, $\mathbf{D}$—diffusion stress strain gauge, $\mathbf{P}$—stress tensor associated with external and internal configuration forces, and dA—integration surface. The expression $\mathbf{f}_{\partial V} \otimes \mathbf{n} + \mathbf{n} \otimes \mathbf{f}_{\partial V}$ describes the phenomena occurring in relation to the issues of transferring the kinetic energy of the drive flow to the sucked-in flow by means of a viscous exchange of the momentum of drops and gas based on the surface mechanism (Duhem, Navier, and du Buat numbers) [109–111].

Some of these mechanisms make the injector work like a compressor. The first type, Witte's shock mixing, is caused by the flow being slowed down when it enters the mixing chamber. Then, there is a change in the nature of the flow from a vortex ring to a spray flow. Before the shock mixing zone, the gas is in a continuous phase while the liquid in the shock mixing zone is in the continuous phase and the gas is dispersed in the form of bubbles. In the shock mixing zone, in a small section of the mixing chamber, the pressure jump occurs [104,105]. There is also a purely oscillating mixing zone, which moves against the flow direction.

Witte's zero-dimensional shock mixing model is based on the flat shock waveform model of compressible fluid. Thus, its main feature is the omission of friction and viscosity as a factor influencing the transfer of energy of the supplying power flow to the suction flow. In this case, the stresses arising in the fluid are described by the term $p\mathbf{I}$. In front of the shock mixing zone, there is a difference in velocity between the liquid and gaseous phase, which is also due to the difference in the kinetic energy of both flows. Beyond the shock mixing zone, the whole kinetic energy difference converts into the compression of the mixture and the kinetic energy of the mixture is below the average kinetic energy of the flows before mixing. This model is relatively easy to implement in 0D CFM (computational flow mechanics) codes.

The second type, Darcy–Weisbach friction mixing [100,106], is based on the incorporation of surface and irreversible phenomena related to viscosity and turbulence into the models. Information about the equation closures is obtained from experiments in which the transfer of kinetic energy from the liquid to gaseous phases is studied using turbulisers that mix both flows. In this case, the velocity uniformity of the two components is stretched in the device space. However, the shape of the first nozzle seems to be the most impor-

tant factor in the turbulence process [112–114]. The friction mixing mechanism favours one-dimensional models of two-phase flows, in which there are a velocity slip, thermal transpiration, and components fraction jump between the phases [109,115]. This velocity slip is described by the additional differential equations [116–118]. Additionally, the components fraction jump takes into account the implementations of numerical codes' more sophisticated boundary conditions [119,120]. Therefore, to correctly describe the individual frictional mixing elements, the Witte model should be extended by $\boldsymbol{\tau} + \mathbf{R} + \mathbf{f}_{\partial V} \otimes \mathbf{n} + \mathbf{n} \otimes \mathbf{f}_{\partial V}$. As mentioned earlier, the transpiration effects can be seen here; then the kinetic energy of the power flow will be transferred to the suction gas. In these phenomena, thermal Reynolds' transpiration is important, as is Graham's component transpiration [109,117].

The third type, Flügel–Cunningham pulse mixing [107,108], unlike the two previous stationary mechanisms, is a pulsed mixing mechanism based on dynamic phenomena occurring within the gripping nozzle and the mixing chamber. The essence of this mechanism is pulsatile compression of the gas occurring in the form of a "plug" occupying the entire cross-section of the mixing chamber. Compression water is present in the form of a movable gas-engaging piston. In the pulsed movement of the piston ("water plug"), the kinetic energy is directly converted into the compressed gas. In other words, Flügel–Cunningham's mechanism assumes that the process of mixing in a liquid-gas ejector involves simultaneous compression and acceleration of the compressed gas stream so that single bubbles are driven into the drive liquid region [121]. In addition, this model is the most similar to the mechanisms caused by steam condensation and it is necessary to take into account the phenomena associated with diffusion and phase transitions caused by external and internal configuring forces, i.e., $\mathbf{D} + \mathbf{P}$, respectively [109–111].

3.3. Mass, Momentum, and Energy Balance in the Spray-Ejector Condenser

Zero-dimensional calculations of the stationary operation of the spray-ejector condenser, as well as of other flow machines, are based on algebraic models of mass, momentum, and energy balance [122–125].

The apparatus has two inlets and one outlet, so the mass balance is presented as:

$$\dot{m}_{14} + \dot{m}_{2^{bap}} = \dot{m}_5 \tag{14}$$

where $\dot{m}_{14} = \dot{m}_{15}$—water mass flow rate, $\dot{m}_{2^{bap}} = \dot{m}_{3^{bap}}$—gas mixture mass flow rate, and $\dot{m}_5 = \dot{m}_{16}$—mass flow rate at the outlet from the spray-ejector condenser. The mass flow rate of the suction mixture is the sum of the mass flows of the individual components according to the expression:

$$\dot{m}_{2^{bap}} = \dot{m}_{CO_2} + \dot{m}_{H_2O} + \dot{m}_{N_2} = Y_{CO_2}\dot{m}_{2^{bap}} + Y_{H_2O}\dot{m}_{2^{bap}} + Y_{N_2}\dot{m}_{2^{bap}} \tag{15}$$

where Y_{CO_2}—mass fractions of CO_2; Y_{H_2O}—mass fractions of H_2O; and Y_{N_2}—mass fractions of N_2, in points 2^{bap} and 3^{bap}.

The momentum balance is represented by the relationship:

$$\dot{m}_{14}\mathbf{c}_{14} + p_{14}A_{14}\mathbf{n}_{14} + \dot{m}_{2^{bap}}\mathbf{c}_{2^{bap}} + p_{2^{bap}}A_{2^{bap}}\mathbf{n}_{2^{bap}} - \mathbf{R}_{14} - \mathbf{R}_{2^{bap}} - \mathbf{R}_5 = \\ = \dot{m}_5\mathbf{c}_5 + p_5A_5\mathbf{n}_5 \tag{16}$$

where, in addition to the pressures, mass streams, and surface area, the following quantities appear: $\mathbf{c}_{14} = c_{14}\mathbf{e}_x$ represents the average inlet velocity vector to the primary nozzle ($\mathbf{e}_x$ unit vector in axis direction), $\mathbf{c}_5 = c_5\mathbf{e}_x$ is the average outlet velocity vector from the diffuser, $\mathbf{c}_{2^{bap}} = c_{2^{bap}}\mathbf{e}_r$ is the average inlet velocity vector to the suction chamber ($\mathbf{e}_r$ unit vector in radial direction), $\mathbf{n}_{14}$ is the normal vector at the inlet to the primary nozzle, $\mathbf{n}_{2^{bap}}$ is the normal vector at the inlet to the suction chamber, $\mathbf{n}_5$ is the normal vector at the outlet from diffuser, $\mathbf{R}_{14}$ is the friction forces in the area of the primary nozzle, $\mathbf{R}_{2^{bap}}$ is the friction forces in the area of the suction chamber, $\mathbf{R}_5$ is the friction forces in the area of the diffuser, $\mathbf{R}_{16}$ is the friction forces in the area of the mixing chamber, $\rho_{14} = \rho_{water}$ is the density of

water, $\rho_{2^{bap}} = \rho_{gs}$ is the density of the gas mixture, and ρ_5 is the mixture density at the outlet from the spray-ejector condenser.

The third energy balance is expressed by the equation:

$$\dot{E}_{14} + \dot{E}_{2^{bap}} - \dot{m}_{14}\Delta e_{14} - : \dot{m}_{2^{bap}}\Delta e_{2^{bap}} - \Delta\dot{E}_{16} - \dot{m}_5\Delta e_5 = \dot{E}_5 \tag{17}$$

where $\dot{E}_{14}$ is the total energy rate at the inlet to the primary nozzle, $\dot{E}_{2^{bap}}$ is the total energy rate at the inlet to the primary nozzle, $\dot{E}_5$ is the total energy rate at the outlet from the diffuser (it contains the power N_{Ce}, namely, compression power (see Equation 4)), Δe_{14} is the unit loss of energy in the primary nozzle, $\Delta e_{2^{bap}}$ is the unit loss of energy in the suction chamber, Δe_5 is the unit loss of energy in the diffuser, and $\Delta\dot{E}_{16}$ represents the total loss of energy in the mixing chamber. The total energy rates $\dot{E}_{2^{bap}}$, $\dot{E}_5$ include similar components as in Equation (5), but with individual parameters related to the inlet of the suction chamber or to the diffuser outlet, respectively: specific internal energy ($u_{2^{bap}}$; u_5), static pressure ($p_{2^{bap}}$; p_5), density ($\rho_{2^{bap}}$; ρ_5), average height of section ($z_{2^{bap}}$; z_5), and average velocity at the cross-section ($c_{2^{bap}}$; c_5). In turn, $\Delta\dot{E}_{16}$ occurs in the form of a source (or loss), which takes into account the phase change occurring in the shock wave area. Specific internal energy or specific internal enthalpy is a function of either temperature, pressure, mass fraction, vapour quality, or in combination, respectively: $u(T; p; Y; x)$ and $h(T; p; Y; x)$. The energy balance equation is further recalculated, as it is extremely important to determine the condensation process between points 3^{bap} and 16 (Figures 4–7), where the mixing with the driving medium from point 15 also occurs. The overall heat transfer coefficient in the spray-ejector condenser becomes extremely high, and the equation governing both fluids is as follows:

$$\dot{m}_{2^{bap}}\left(h_{3^{bap}} - h_{16}\right) = \dot{m}_{14}(h_{16} - h_{15}) \tag{18}$$

where the enthalpy of characteristic points from Figure 5 appears—namely, the specific enthalpy of gases behind the suction chamber ($h_{3^{bap}}$), the specific enthalpy of water flowing out of the primary nozzle (h_{15}), and the specific enthalpy of the water-gas mixture flowing out of the mixing chamber of the spray-ejector condenser (h_{16}). It should be added that the enthalpy in point 16 is determined by several parameters, namely:

the mass entrainment ratio χ_m, which has a similar function to that of the water circulation rate of cooling water in the classical turbine condenser and the cooling tower;

the location of point 16 to the left of the saturated liquid ($x = 0$), as in Figure 4; and

the process of CO_2 compression and volumetric entrainment ratio χ calculated in relation to the fraction of CO_2 contained in the mixture.

However, the value of χ_m should provide the accurate level of the volumetric entrainment ratio χ, mainly $\chi \approx 1$, which is typical for appropriately designed water-gas ejectors [94].

3.4. Velocity Relations with Respect to Momentum and Energy Balances

Ejectors are unusual devices in which the relationship between pressure and velocity plays an essential role. Unlike with other engineering design modelling devices, it is necessary to determine the kinetic energy and the main component of the average velocity vector (c). The zero-dimensional modelling of a stationary ejector consists of preserving the formulas for its individual components, which act as confusers (nozzles), a mixing heat exchanger, and, in the last section, a diffuser.

The reference average velocity on which the modelling is based is called the ideal supply velocity c_{15i}. Authors estimate it as if there were no suction working fluid in the suction chamber. In other words, c_{15i} is an ideal quantity in which index (15) means supply and index (i) represnts the initial state ($\dot{m}_{2^{bap}} = 0$) at which this velocity is calculated:

$$c_{15i} = \varphi_{nt}\sqrt{2\left(\frac{p_{14}}{\rho_{14}} - \frac{p_{2^{bap}}}{\rho_{2^{bap}}}\right)} \tag{19}$$

where $\varphi_{nt} \approx 0.95 - 0.99$ is the theoretical velocity coefficient in the primary nozzle. This theoretical velocity is also referred to as Flügel velocity [94]. It allows for the determination of other velocities in characteristic sections: c_{15}, $c_{3^{bap}}$, c_{16}, or c_5.

First, let us determine the average flow velocity in the outlet section of the primary nozzle, corresponding to the pressure drop $p_{14} - p_{3^{bap}}$. In the first approximation, c_{15} is obtained from closing in accordance with the following relation:

$$c_{15} = \varphi_n \sqrt{2\left(\frac{p_{14}}{\rho_{14}} - \frac{p_{3^{bap}}}{\rho_{14}}\right)} \tag{20}$$

where $\varphi_n = 0.92 - 0.95$ represents the real velocity coefficient in the primary nozzle. However, in the case of high velocities at the inlet to the primary nozzle, the input from the kinetic energy $\frac{1}{2}c_{14}^2$ should be considered, which contributes to the energy balance and, finally, leads to c_{15} as described by the formula:

$$c_{15} = \varphi_n \sqrt{2\left(\frac{p_{14}}{\rho_{14}} - \frac{p_{3^{bap}}}{\rho_{14}}\right) + c_{14}^2} \tag{21}$$

Second, the average velocity of the gaseous mixture in the ring cross-section $A_{3^{bap}}$, usually corresponds with the pressure drop $p_{2^{bap}} - p_{3^{bap}}$ and is equal:

$$c_{3^{bap}} = \varphi_{sc} \sqrt{2\left(h_{2^{bap}}{}^t - h_{3^{bap}}{}^t\right)} \tag{22}$$

where $\varphi_{sc} = 0.92 - 0.95$ represents the velocity coefficient in the suction chamber, $h_{2^{bap}}{}^t = h_{2^{bap}}{}^t\left(T_{2^{bap}}, p_{2^{bap}}, Y_{2^{bap}}\right)$ represents the total enthalpy of the suction mixture gas (cross-section 2^{bap}—Figure 8), and $h_{3^{bap}}{}^t = h_{3^{bap}}{}^t\left(T_{3^{bap}}, p_{3^{bap}}, Y_{3^{bap}}\right)$ enthalpy of the suction mixture in cross-section $A_{3^{bap}}$. The average velocity $c_{3^{bap}}$ for the spray-ejector condenser is also described by the equation:

$$c_{3^{bap}} = \varphi_{sc} \sqrt{2\left(\frac{p_{2^{bap}}}{\rho_{2^{bap}}} - \frac{p_{3^{bap}}}{\rho_{3^{bap}}}\right) + c_{2^{bap}}^2} \tag{23}$$

where $c_{2^{bap}}^2$ represents input from the kinetic energy in the suction chamber.

Third, when determining the average velocity at the outlet of the mixing chamber, the transformed equation of momentum balance can be used:

$$c_{16} = c_{4^{bap}} = \eta_{MC} \frac{c_{15}\dot{m}_{14} + c_{3^{bap}}\dot{m}_{2^{bap}}}{\dot{m}_{14} + \dot{m}_{2^{bap}}} \tag{24}$$

where $\eta_{MC} = 0.95$ expresses the mixing efficiency in the mixing chamber.

Fourth is the average velocity at the exit of the diffuser, which is also included in the momentum balance (16). It is initially determined by means of a relationship:

$$c_5 = \varphi_d \sqrt{2\left(\frac{p_5}{\rho_5} - \frac{p_{16}}{\rho_{16}}\right) + c_{16}^2} \tag{25}$$

where $\varphi_d = 0.93$ represents the velocity coefficient in the diffuser.

While solving the three balance Equations (15)–(17), the basic values at the outlet of the spray-ejector condenser can be obtained—namely, $\dot{m}_5$, c_5, and T_5. In addition, specific total enthalpy $h_5{}^t$ and the associated temperature T_5 should fulfil the equation:

$$c_5 = \varphi_d \sqrt{2[h_5{}^t(p_5, T_5, Y_5) - h_{16}{}^t(p_{16}, T_{16}, Y_{16})]} \tag{26}$$

3.5. Closures for the Spray-Ejector Condenser

An important issue is the selection of appropriate closures and constants in individual equations adopted for analysis. The unit compression work based on the pressure increase in the diffuser can be calculated following Cunningham [94,107,108]:

$$w_{16,5r} = \frac{\dot{m}_{sg(16)}}{\dot{m}_5} RT_{16} \ln\left(\frac{p_5}{p_{16}}\right) + \frac{\dot{m}_{H_2O(l)}}{\dot{m}_5} v_{16}(p_5 - p_{16}) \tag{27}$$

where v_{16}—specific volume in point 16, R—individual gas constant, T_{16}—temperature in point 16, and other quantities as described in the Equations (7) and (14)–(17).

Most geometric sizes can be determined secondarily by substituting values to the transformed mass continuity equation. For example, the surface is defined as:

$$A = \frac{\dot{m}}{\rho c} \tag{28}$$

However, in the case of a spray-ejector condenser, it will be important to check the individual coefficients in a dedicated benchmarking experiment. Important data obtained during such a measurement campaign are local drag coefficients linked simultaneously to the physics of two-phase and multi-component flows. While determining this value for a single driving nozzle seems to be a triviality, as water itself flows there, for more sophisticated shapes the frictional resistance force is defined as:

$$\mathbf{R}_{14} = \frac{1}{2}\xi_{14}\rho_{14}c_{14}^2 \, A_{14} \, \mathbf{e}_x \tag{29}$$

where ξ_{14} is the local loss coefficient for the new type of confuser that should be thoroughly investigated, A_{14} is the total primary nozzle inlet area, and $\mathbf{e}_x$ is the unit vectors in the axis direction. The remaining coefficients should be examined more precisely to correctly determine the drag force in the suction chamber:

$$\mathbf{R}_{2^{bap}} = \frac{1}{2}\xi_{2^{bap}}\rho_{2^{bap}}c_{2^{bap}}^2 \, A_{2^{bap}} \, \mathbf{e}_r \tag{30}$$

where $\xi_{2^{bap}}$ the coefficient of local losses for the suction chamber should include processes in the suction chamber and atypical change of flow direction from the radial (according to $\mathbf{e}_r$ and attached to the sidewall $A_{2^{bap}}$) to the axial direction $\mathbf{e}_x$ on the annular surface $A_{3^{bap}}$. The drag force in the diffuser should then be determined:

$$\mathbf{R}_5 = \frac{1}{2}\xi_5\rho_5c_5^2A_5 \, \mathbf{e}_x \tag{31}$$

where ξ_5 is the coefficient of local losses in the diffusor and A_5 is the diffuser outlet surface. The last drag force occurring inside the spray-ejector condenser is that of the secondary nozzle and mixing chamber:

$$\mathbf{R}_{16} = \frac{1}{2}\xi_{16}\rho_{16}c_{16}^2A_{16} \, \mathbf{e}_x \tag{32}$$

where ξ_{16} is the generalised local loss factor and A_{16} is the cross-section of the mixing chamber. This approach is used in this article. In addition, pressure closures behind the mixing chamber allow the pressure p_{16}:

$$p_{16} = p_{3^{bap}} - \frac{1}{2}k_{MC}\rho_{3^{bap}}\left(c_{15} + c_{3^{bap}} - c_{16}\right)^2 \tag{33}$$

where k_{MC} represents a coefficient of friction. However, due to the most complex flow structure of the secondary nozzle and mixing chamber, where condensation, mixing, dif-

fusion, and velocity slip between phases, effects occur leading to thermo, concentration, phase, and pressure transpiration. It is reasonable to write the equation:

$$\mathbf{R}_{16} = \left\{ \nu_{Du} p_{16} + \nu_{Na} c_{16} + \nu_B \rho_{16} c_{16}^2 \right\} A_{16} \mathbf{e}_x \\ - (\beta_{mT} \text{grad}_s T + \beta_{mY} \text{grad}_s Y + \beta_{mx} \text{grad}_s x + \beta_{mp} \text{grad}_s p) \tag{34}$$

where quantities appear, such as ν_{Du}, ν_{Na}, and ν_B are the adherence (Duhem), slip (Navier), and kinetic (du Buet) parts surface friction coefficients, respectively; $\beta_{mT}, \beta_{mY}, \beta_{mx}$, and β_{mp} are the mobility coefficients of thermal transpiration, diffusion-phoresis, phase-phoresis, and pressure transpiration, respectively; and grad_s represents the two-dimensional surface gradient [75,109,120].

Another issue involves closures for temperatures inside the spray-ejector condenser, namely:

$$T_{15} = T_{15}(h_{15}; p_{15}) \tag{35}$$

where authors use the tables built into the calculation programs. Then, the temperatures of the mixture can be obtained as follows:

$$T_{3^{bap}} = T_{3^{bap}}\left(h_{3^{bap}}; p_{3^{bap}}; Y_{3^{bap}}\right) \tag{36}$$

$$T_{16} = T_{16}(h_{16}; p_{16}; Y_{16}) \tag{37}$$

where $Y_{3^{bap}} = Y_{2^{bap}} = Y_{2^{bap}}\left(Y_{CO_2}; Y_{H_2O}; Y_{N_2}\right)$ and $Y_{16} = Y_{16}\left(Y'_{CO_2}; Y'_{H_2O}; Y'_{N_2}\right)$. However, in the case of mass fractions in point 16, other values resulting from the relationship can be obtained:

$$\dot{m}_{16} = \dot{m}_{4^{bap}} = \dot{m}_5 = \dot{m}'_{CO_2} + \dot{m}'_{H_2O} + \dot{m}'_{N_2} = Y'_{CO_2} \dot{m}_{16} + Y'_{H_2O} \dot{m}_{16} + Y'_{N_2} \dot{m}_{16} \tag{38}$$

In Equation (37), enthalpy was determined from Equation (18). Individual specific enthalpy from Equations (35) and (36) was established based on the efficiency of the internal devices as follows:

$$h_{15} = h_{14} - \eta_n(h_{14} - h_{15_s}) \tag{39}$$

$$h_{3^{bap}} = h_{2^{bap}} - \eta_{sc}\left(h_{2^{bap}} - h_{3^{bap}_s}\right) \tag{40}$$

where η_n is the nozzle isentropic efficiency and η_{sc} is the expansion in the suction chamber isentropic efficiency. In a classic two-phase ejector, the motive medium (most often water) circulates and is circulated, while its temperature within a relatively short time after start-up is adjusted to the temperature of the sucking gas [26,55–58]. In this work, the motive medium is cooled in S+CHE (separator and condensate cooling heat exchanger). Therefore, water has a constant temperature of about 25 °C, which means the temperature difference always occurs as an additional driving medium for both flow and condensation.

3.6. Efficiency and Power Output

The electrical power output of DBCOCC has been defined based on the electrical efficiency of the generator η_G, or electric motors and the mechanical power of individual thermal circulation devices, such as gas turbine P_{GT}, compressor P_C, and circulating water paper P_P. Thus, the electrical power of the entire system P_{el}, together with the electrical power demand of the ASU station P_{el-ASU}, with the carbon dioxide capture unit demand P_{el-CCU}:

$$P_{el} = P_{el-DBC} - P_{el-ASU} - P_{el-CCU} \tag{41}$$

where P_{el-DBC} occurs including pump power P_{el-P} according to the equation:

$$P_{el-DBC} = \eta_G(P_{GT} - P_C) - \eta_M P_P \tag{42}$$

where η_G is the efficiency of the electric generator and η_M is the efficiency of the electrical motor. The power required to drive the compressor, P_C, is calculated by the following relationship [73,74]:

$$P_C = \dot{m}_1 \, \eta_{mC} \, (h_1 - h_2) \tag{43}$$

where $\dot{m}_1$ is the mass flow rate of oxygen from the ASU station, η_{mC} is the mechanical efficiency of the compressor, and h_1 : and h_2 is the specific enthalpy at individual points. To determine the specific enthalpy of the working fluid at characteristic points, thermodynamic tables are necessary.

Furthermore, in the air separation unit (ASU) and carbon capture unit (CCU), compressors are an element that reduces electrical power in a similar way. The compression of carbon dioxide is more complex, thus it is worth defining the power consumed by the CCU for this process:

$$P_{el-CCU} = \eta_M \eta_{mC} \left[\dot{m}_6 \left(h_{1CCU} - h_6 \right) + \dot{m}_{3CCU} \left(h_{4CCU} - h_{3CCU} \right) + \dot{m}_{6CCU} \left(h_{7CCU} - h_{6CCU} \right) \right] \tag{44}$$

where $\dot{m}_6$, $\dot{m}_{3CCU}$, and $\dot{m}_{6CCU}$ are the mass flow rates of the mixture at the inlet to the first, second, and third CO_2 compressors, respectively; and $h_{1CCU} - h_{6CCU}$ is the specific enthalpy at each point.

The power of turbine P_{GT} is determined from the following relation:

$$P_{GT} = \dot{m}_3 \left[\left(h_3 - h_4 \right) + \left(h_4 - h_{1^{bap}} \right) \right] \eta_{mGT} \tag{45}$$

where η_{mGT} is the mechanical efficiency of a gas turbine; $h_3, h_4,$ and $h_{1^{bap}}$ is the specific enthalpy at individual points; and $\dot{m}_3$ is the mass flow rate at point 3. In Equation (32), the power of the water pumps (N_P) supplying both the wet combustion chamber and the spray-ejector condenser appears. The total power of the pumps (P$_1$ and P$_2$) is determined by as follows:

$$P_P = \dot{m}_8 v_8 (p_9 - p_8) + \dot{m}_{13} v_{13} (p_{14} - p_{13}) = \dot{V}_8 (p_9 - p_8) + \dot{V}_{13} (p_{14} - p_{13}) \tag{46}$$

where the thermodynamic parameters occur: v—specific volume, p—pressure, $\dot{m}$—mass flow rate, and $\dot{V}$—volume flow rate.

In addition to the thermodynamic parameters that affect the operation of the cold sub-cycle, it is important that $T_{3^{bap}}$ affects the performance of the entire block. Ultimately, the DBCOCC efficiency can be calculated as indicated below:

$$\eta_{el} = \frac{P_{el}}{\dot{m}_f LHV} \tag{47}$$

where LHV represents low heating value, $\dot{m}_f$ mass flow rate of fuel, and N_{el} represents Equation (41).

3.7. Simplifications and Assumptions Adopted for the Model

With respect to DBCOCC, the calculations of this model were based on the simplifications and assumptions presented in Table 1. Relative pressure losses were considered. The minimum temperature on the cold side equals 70 K. The proposed mathematical models were verified in several articles—namely, for the gas-steam unit in [73], for the gas cycle with heat regeneration in article [74], for nuclear systems with gas cycles in article [126], for systems with water-gas ejectors in articles [8,90], for steam units in articles [127,128], and for inversed Brayton cycle in article [129]. Based on previous experience and verification at the power plants with a measurement base, it was found that the calculations were of sufficient accuracy. On the basis of CFM tools, a new type of cycle can be designed including DBCOCC. The assumed efficiencies are presented in Table 1. The results presented in Section 4 were obtained for the ambient conditions contained in Table 1, and in particular for the fuel, air, and condenser cooling water parameters.

Table 1. Inlet parameters of DBCOCC.

Parameter	Symbol	Unit	Value	Reference
Efficiency and pressure drop in main devices				
Mechanical efficiency of the turbine and compressor	η_{mGT} ; η_{mC}	-	0.99	[1,5]
Isentropic efficiency of the turbine	η_{iGT}	-	0.89	[1,5]
Isentropic efficiency of the compressor	η_{iC}	-	0.88	[1,5]
Electrical motor efficiency	η_M	-	0.95	[1,5]
Electrical generator efficiency	η_G	-	0.97	[1,5]
Relative pressure losses in the combustion chamber	$\Delta p_{2-3}/p_2$	-	0.003	[1,5]
Efficiency of the combustion chamber with $T_{TIT} = T_{3'} = 1373.15$ (K)	η_{CC}	-	0.99	[129]
Isentropic efficiency of pump	η_{iP}	-	0.75	[1,5]
Mechanical efficiency of pump	η_{mP}		0.98	[1,5]
Thermal efficiency of cooling heat exchangers	η_{CHE}		0.98	[1,5]
Relative pressure losses in regenerative heat exchangers HE				
HE—the low-temperature (cold) side	$\Delta p_{1^{bap}-2^{bap}}/p_{1^{bap}}$	-	0.006	[130]
HE—the high-temperature (hot) side	$\Delta p_{9-10}/p_9$	-	0.0075	[130]
Minimum temperature difference	ΔT_{HE}	K	70	[130]
Air and fuel thermodynamic parameters				
Fuel temperature	T_f	K	288.15	[1,5]
Fuel pressure	p_f	MPa	4.05	[1,5]
Fuel mass flow rate	$\dot{m}_f$	kg/s	12.83	[129]
Air temperature	T_{air}	K	288.15	[1,5]
Air pressure	p_{air}	MPa	0.101	[1,5]
Oxygen mass flow rate	$\dot{m}_{O_2}$	kg/s	51.8	[129]
Spray-ejector condenser				
Volumetric entrainment ratio	χ	-	1	[94]
Pressure ratio with regard to pressure at the outlet from the spray-ejector condenser	π_{sc}	-	64.1	[94]
Dimensionless compression ratio	Π_c	-	0.19748	[94]
Efficiency of the nozzle	η_n	-	0.91	[94]
Efficiency of the suction chamber	η_{sc}	-	0.99	[94]
Efficiency of the secondary nozzle and mixing chamber	η_{MC}	-	0.99	[94]
Efficiency of the diffuser	η_d	-	0.7	[94]
Assumed parameters in thermodynamic points				
Water injected to combustion chamber mass flow rate	$\dot{m}_{10} = \dot{m}_9 = \dot{m}_8$	kg/s	117.7	[129]
Temperature of condensation	T_5	°C	20	[129]
Pressure at the outlet from the CCU	p_{7CCU}	bar	80	[129]
Pressure at the outlet from the turbine	$p_{3^{bap}}$	kPa	7.7	[129]
Pressure of condensation	$p_{2^{bap}}$	kPa	7.0	[94]

4. Results of Thermodynamic Analysis

Thermal cycle calculations were made for constant flows of fuel, water, and oxygen injected into the combustion chamber, in such a way that total flue gas through the turbine

was 182.3 kg/s. The adopted pressure was constant and equal to 40 bars. Furthermore, the temperature difference in the HE regeneration exchanger was assumed to be around 70 K in order to keep the system compact, while condensation temperature was 20 °C (Table 2).

Table 2. Thermodynamic parameters and molar fractions at individual points of Brayton's dual cycle at condensation pressure p_{3in} = 7.8 kPa.

Point	T	p	x	$\dot{m}$	Mole Fraction X				
					O_2	H_2O	N_2	CO_2	NO_X
	°C	kPa	-	kg/s	-				
1	32.2	515.8	1.00	51.8	0.989	0.000	0.011	0.000	0.000
2	822	4050.0	1.00	51.8	0.989	0.000	0.011	0.000	0.000
3	1338	4000.0	1.00	182.3	0.000	0.908	0.002	0.089	0.000
4	641	101.3	1.00	182.3	0.000	0.908	0.002	0.089	0.000
1^{bap}	302	7.7	1.00	182.3	0.000	0.908	0.002	0.089	0.000
2^{bap}	101	7.7	1.00	182.3	0.000	0.908	0.002	0.089	0.000
3^{bap}	39.0	7.0	0.93	182.3	0.000	0.9084	0.0022	0.0894	0.000
4^{bap} = 16	20.83	7.0	0.001	159,192.0	-	1 (lq)	-	-	-
5	20.83	101.3	0.001	159,192.0	-	1 (lq)	-	-	-
6	20	101.3	1.00	36.4	0.000	0.042	0.024	0.934	0.000
7	20	101.3	0.00	159,155.6	0.000	1 (lq)	0.000	0.000	0.000
8	20	101.3	0.00	159,155.6	0.000	1 (lq)	0.000	0.000	0.000
9	20.05	4000.0	0.00	117.7	0.000	1 (lq)	0.000	0.000	0.000
10	214	4000.0	0,00	117.7	0.000	1 (lq)	0.000	0.000	0.000
11	20	101.3	0.00	159,037.9	0.000	1 (lq)	0.000	0.000	0.000
12	20	101.3	0.00	28.2	0.000	1 (lq)	0.000	0.000	0.000
13	20	101.3	0.00	159,009.6	0.000	1 (lq)	0.000	0.000	0.000
14	20.1	500.0	0.00	159,009.6	0.000	1 (lq)	0.000	0.000	0.000
15	20.1	7.0	0.00	159,009.6	0.000	1 (lq)	0.000	0.000	0.000
1^{CCU}	151	500.0	1.00	36.4	0.000	0.042	0.024	0.934	0.000
2^{CCU}	30	500.0	0.00	0.526	0.000	1 (lq)	0.000	0.000	0.000
3^{CCU}	30	500.0	1.00	35.91	0.000	0.009	0.022	0.969	0.000
4^{CCU}	172	2500.0	1.00	35.91	0.000	0.009	0.022	0.969	0.000
5^{CCU}	30	2500.0	0.00	0.099	0.000	1 (lq)	0.000	0.000	0.000
6^{CCU}	30	2500.0	1.00	35.81	0.000	0.002	0.023	0.975	0.000
7^{CCU}	138	8000.0	1.00	35.81	0.000	0.002	0.023	0.975	0.000

In the thermodynamic analysis, individual nodal points of the circulation of both the entire system $\eta_{el-netto}$ and its individual parts were examined. The results of the analysis are presented in Table 2. Several points can be distinguished in which the separation of water from the rest of the medium occurs. The highest mass flow rate is at point 12 and amounts to 28.2 kg/s, which is over 95% of all water produced during methane combustion. Some quantities are additionally separated in the CCU and are 0.5 kg/s at point 2^{CCU} of the CCU and 0.1 at point 5^{CCU}, respectively. It is worth noting that the total efficiency of the system is $\eta_{el-netto}$ = 37.78%.

Carbon dioxide capture from flue gas consisting only of steam and carbon dioxide (modelled in this work) is simpler and more cost-effective than other methods used for CCS, i.e., post-combustion and precombustion [35]. The energy intensity of the modelled oxygen generating station (ASU) is β = 0.248 kWh/kgO$_2$ (for comparison, the value of the energy intensity at work [38] is β = 0.247 kWh/kgO$_2$, while at work [40] it is β = 0.250 kWh/kgO$_2$). Oxygen goes to the wet combustion chamber, where stoichiometric combustion of methane occurs. The water circulates in a similar way as it does in Rankine's closed cycles. Assumptions for analyses are presented in Table 1 and examples of node points at maximum efficiency are collected in Table 2.

To keep the whole system compact, an important device in the cycle is the CO_2/water separator, which in this case will be a centrifugal separator. The gases separated after condensation are H_2O, CO_2, and N_2, where the molar share of the CO_2 obtained is 0.975.

The analysis carried out in the previous article has shown that introduction of the inversed Brayton cycle (IBC) increases the system's power [129]. The highest net efficiency $\eta_{el-netto} = 43.67\%$ was obtained at condenser pressure $p = 0.078$ kPa. An unquestionable advantage of the solution presented in Ziółkowski's paper [8], with the use of oxy-combustion and carbon dioxide capture, is the lack of emission of pollutants, such as nitrogen oxides and carbon dioxide. As a result of producing oxygen, efficiency falls by 6.38%. Then, after capturing CO_2, it falls by another 2.28%. In this article, the analyses were extended to include a new element—the spray-ejector condenser, which ensured compactness. The extension of information about the parameters at the nodal points of the spray-ejector condenser sub-circulation is collected in Table 3.

Table 3. The thermodynamic parameters of the medium and operational values at characteristic points of the cold sub-cycle at the turbine outlet pressure of $p_{2^{bap}} = 7.8$ kPa.

Point	T	p	c	h_c	h	$\dot{m}$	$\dot{V}$	A	ρ
	°C	bar	m/s	kJ/kg	kJ/kg	kg/s	m³/s	m²	kg/m³
2^{bap}	101.0	0.078	50.00	1.25	3080.79	182.3	5216.8	104.34	0.03494
3^{bap}	39.0	0.07	559.19	156.35	2571.76	182.3	1773.9	3.17	0.10277
14	20.0	5.00	100.00	5.00	126.20	145,332.3	145.9	1.46	995.82
15	20.0	0.07	104.84	5.50	125.75	145,332.3	145.9	1.39	995.82
$4^{bap} = 16$	20.83	0.07	100.13	5.01	129.48	145,514.6	146.2	1.46	995.33
5	20.83	1.05	99.14	4.91	129.66	145,514.6	146.2	1.47	995.37

To address the most important device in this sub-cycle, i.e., the spray-ejector condenser (SEC), design of which is based, mainly, on the equations describing ejectors, it is necessary to distinguish the characteristic junction points presented in Figures 4–7, in which thermodynamic parameters were determined based on equations of conservation of mass, momentum, and energy. Thermodynamic analysis results define the efficiency of a system using oxy-fuel combustion and carbon capture.

As to the velocities themselves, in a 0D approach, average cross-section velocities rather than profiles are determined. Due to a wide discrepancy between velocities set in calculations for traditional ejectors ($c = 0$ m/s) and outlets of traditional turbines (up to $c = 300$ m/s), there is a considerable gap. Therefore, the velocity of steam movement has been drawn from the literature [131]: $c = 50$ m/s and [132,133]: $c = 100 - 200$ m/s.

Presented below are analysis results obtained using an in-house code. The cycle schematic diagram for the compact high-efficiency zero-emission power plant is presented in Figure 1. The calculations retain efficiency values for the compressor and turbine presented in Table 1. To correctly determine the momentum balance, it is necessary to assume the velocity at the inlet to the primary nozzle and suction chamber.

Calculated results for the thermal sub-cycle in which the ejector operates at $c_{2_a^{in}} = 50$ m/s velocity of the gas-and-steam mixture entering the suction tap (into the suction component of the condenser) and $c_{11} = 100$ m/s velocity of the supply working fluid are presented in Table 2. Additional assumptions concerning the calculations obtained for the case under consideration are the suction pressure determinant and the volumetric degree of ejection, and they are gathered in Table 1. The pressure has been assumed to be 103.1 kPa at the outlet from the diffuser due to a lack of ejector characteristics, thereby removing the compressor from among the cycle components.

Authors also designed the flowpath of analysed turbine. Mass flow rate is $\dot{m} = 182.3$ kg/s which is similar to the mass flow in the GT8C gas turbine. Nevertheless, gases expanding inside turbine consist mostly of steam vapour. Because of that, geometry of designed turbine is much more similar to steam turbines than to gas turbines. Figure 9 shows the shape of the

high-pressure turbine flow channels. It is worth mentioning that length of mean diameter and blade length is significant throughout the high-pressure part. Change of diameters is more prominent than in conventional high-pressure steam turbine casings. Figure 10 presents the shape of the low-pressure turbine flow channels. They were designed through calculation of the stages. The increase of the mean diameter and blade length can be observed, especially in the case of the low-pressure part. The shape of the channel does not differ much from a conventional steam turbine. The blades of the last stage have extreme length—157 cm. Blades of similar length have been put into service in Kozienice Power Plant in Poland. The usage of such long blades results in a substantial outlet area (18.06 m^2), which allows reducing of the number of low-profile casings from 4 to 2. This change means lower potential investment costs of the turbine.
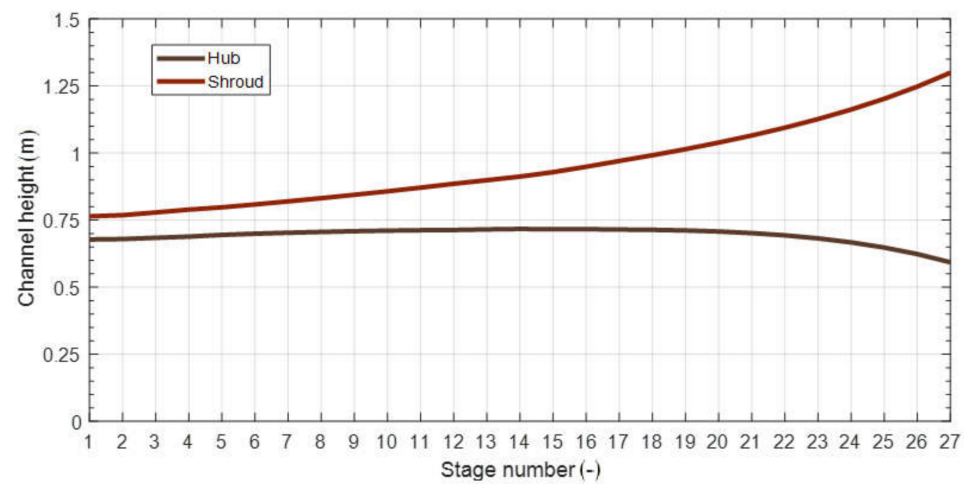
Figure 9. High-pressure turbine flow channel.
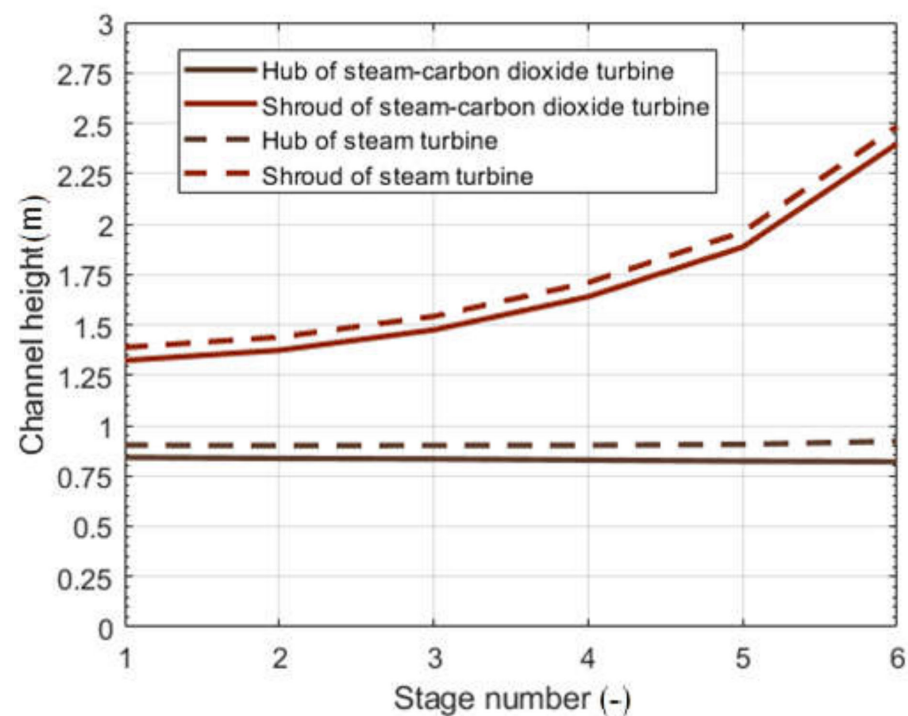
Figure 10. Comparison of LP channel geometries.

It is important to determine the progress of condensation between points $2^{bap} - 4^{bap} - 16$ (Figures 3–7), where mixing with the propeller medium from points 15 and 2^{bap} to 16 takes place. The entire heat transfer process in the spray ejector condenser occurs at an extremely

high heat transfer coefficient—namely, it can reach as much as 1,000,000:W/(m²K) [134], whereas in a traditional condenser heat transfer coefficient usually ranges from 2300 to 4500:W/(m²K) [131].

Based on the following assumptions, calculations were made, and the operating point was determined for the gas and steam turbine cycle with a spray ejector condenser. The analysis of the results in Table 3 should focus particularly on the velocity value obtained in the area of the suction nozzle area, which in this case equals approximately 1.2 Mach. The medium can attain this speed because of condensation occurring in the water drops in the spray ejector condenser. That the condensation may be exploited at such high velocities is noteworthy because these values are encountered in other types of devices and applications, and efforts are usually made to eliminate them. It should be noted that the shock wave appears in the last stages of steam turbine nozzles [135], in two-phase steam ejectors [134]. These phenomena are considered to be negative due to the emission of noise and vibrations [136,137].

Velocities of 559.19 m/s have been calculated in spray-ejector condensers at point 3^{bap} (Table 3). A Mach number for this mixture of 1.2 was obtained according to COM-GAS and 1.36 according to Refprop. Both values are higher than 1 Mach. In these conditions supersonic shock waves occur due to supersonic flow. This value also results from the speeds assumed at the SEC inlet. More information about working fluid velocity at the outlet of the turbine, before suction nozzle, can be found in publications [37,138,139]. Velocity is high due to conditions at the last stage with extremely long blades (1.8 m). It is easier to achieve slower fluid velocity in smaller turbines; however, fluid velocity can reach 370 m/s even in small turbines, a value close to the speed of sound in conditions at the outlet of the turbine [140–142].

The resulting shock wave has a strongly dissipative effect that is desirable in an ejector only in the mixing chamber area, where it ensures compression of the medium. However, condensation in a spray ejector condenser occurs as a result of the shock wave, which shortens the distance necessary for the water to condensate out of the steam and gas mixture. This is a positive development. Furthermore, note should be taken of a shift in the shock wave receding from the centre point of the mixing chamber area towards the borderline between the suction and mixing chambers. Therefore, an increase in pressure is the product of forces exerted by the shock wave and the diffuser process.

As shown in Figures 3–7 and Tables 1–3, condenser outlet pressure should be taken to equal around 101.3 kPa, as is the case with water-gas ejectors. For example, water-gas ejectors are installed in 12 blocks of the Bełchatów power plant and their task is to extract air from steam turbine condensers. As in the example below, they transport gases from a negative pressure of the order of 0.04–0.1 bar to atmospheric pressure present in the supply water tank [90].

Provided that the design assumptions and parameters shown in Table 1 are met, the spray ejector condenser efficiency equals 10%, which is not significant compared to existing ejectors usually operating in the efficiency range of 8–40%. Dedicated experiments would be in order to find out whether the condenser operates in the lower or upper range of ejector efficiency. This analysis adopts a safer solution.

5. Discussion—Compactness of the Steam Generator Condenser and Gas-Steam Turbine

At the same time, it should be realized that energy conversion is enhanced due to the reduced size of the device, as shown by the following formula describing heat flux density:

$$q = \frac{\dot{Q}}{V'} \tag{48}$$

where $\dot{Q}$ is heat flux transferred within the device and V is device volume.

5.1. Spray-Ejector Condenser

Typical condensers provide heat flux densities of around $q = 180$ kW$_t$/m^3. On the other hand, in the case of a spray ejector condenser (SEC), the same value in Figure 1 stands at $q = 5800$ kW$_t$/m^3. This means that energy conversion has been enhanced by around 32 times in the lower heat source area. However, these concerns require further research and calibration on dedicated workstations. It should also be mentioned that a certain analogy exists in the case of vapour-liquid ejectors operating in left-handed cooling cycles in which another parameter related to heat exchange, i.e., heat transfer coefficient, is equal to $\alpha = 1,000,000$ W/(m^{2}K) [134], while a traditional condenser oscillates from $\alpha = 2300$ W/(m^{2}K) to $\alpha = 4500$ W/(m^{2}K) [91,131].

5.2. Wet Combustion Chamber

Relatively high efficiency has been achieved for cycles with a wet combustion chamber due to the replacement of the air compressor with a water pump. With adequately selected parameters, an adjustment for flow through porous structures will slightly improve the cycle efficiency, or at least decrease the estimated friction caused by various types of membranes. An essential benefit of the device under consideration is provided by its compact size, as proved by the following formula illustrating heat flux density (6).

Table 4 presents a comparison of the major parameters of boilers and wet combustion chambers, where $\dot{Q}$ denotes heat flux in the device, while V stands for the device's volume. In typical steam boilers (B) or heat recovery steam generators (HRSG), heat flux density stands at $q_B = 7.9$ kW$_t$/m^3 and $q_{HRSG} = 109$ kW$_t$/m^3, respectively. However, in the case of considering only the water wall, the heat flux density will equal $q_{B\ water\ wall} = 105$ kW$_t$/m^3. A wet combustion chamber, on the other hand, delivers heat flux densities of $q_{WCC} = 3358$ kW$_t$/m^3. Therefore, the enhancement of energy conversion in the upper heat source area can even be 30-fold.

In comparing the obtained results to the reference data [143,144], it is to be expected that a new state of structural tension will be observed relative to the currently investigated devices, such as boilers and steam turbines. It will probably be necessary to introduce a new definition of stress tensor in a porous structure to take into account not only the impact of mechanical tension but also of the impact of the temperature gradient, different levels of component concentration, and sorption in the active area of the pores [145].

Table 4. A comparison of the main parameters of a heat recovery steam generator (HRSG) and a steam boiler (B) PB 1100, and a wet combustion chamber (WCC).

Type of Steam Generator	Reference	V	$\dot{Q}$	q
		m^3	MW$_t$	kWt/m^3
HRSG	[131]	1008	110.00	109.13
B	[146–148]	87,480	694.40	7.94 (109)
WCC	This research	160	537.28	3358.02

The reduction alone of the device size, with the appropriate heat flux transfer, is also sought in the field of heat exchangers, the volume of which may shrink up to 20 times as a result of micro-canals used, for example, in scored boards. Examples of research on, and the design of, compact and conventional heat exchangers are among the areas of activity of other authors [126,146–150].

5.3. Gas-Steam Turbine

Authors also designed an equivalent low pressure turbine part which operates only on water steam. Figure 10 presents a comparison of geometries of low-pressure channels for pure steam and mixture variants. Expansion for both turbines starts at equal pressure (119 kPa) and temperature (622.8 °C), and ends at the same pressure (7.9 kPa). Their geometries are similar, but specific enthalpy drop in the pure steam version is 12% higher

than in the mixture variant. This mean that the specific work per kilogram of gas is lower in the mixture variant. Forces acting on blades and thus force momentum on the turbine shaft are smaller in the mixture turbine. The specific volume of steam-carbon dioxide mixture is slightly lower than in the pure steam version, but gas reached higher velocities in the steam channel. As a result, for equal last-stage blade lengths the exhaust loss is lower in the H_2O-CO_2 mixture version. Usage of this mixture makes it possible to reduce the exhaust loss or to use shorter last-stage blades for equal mass flow rate in comparison with steam, but the power of this turbine is also lower. For turbines with the same power, the steam variant would have slightly shorter last-stage blades than the mixture variant.

6. Conclusions and Perspectives

This paper provides an overview of oxy-fuel combustion systems and a description of the compact high efficiency and zero-emission power plant with carbon capture. The numerical analysis of the thermal cycle is carried out by in-house COM-GAS program. In order to do quick and multiple calculations of the compact high efficiency and zero-emission power plant with carbon capture during the multivariant design process, a computer code combined with so-called friendly use of graphical mode for preparation and change of a given scheme of the cycle has been developed. The in-house COM-GAS code algorithm is based on the fulfilment of the basic governing balances of mass, momentum, and energy at discrete points of the cycle.

The main novelty is integration of the spray-ejector condenser and wet combustion chamber to obtain a compact power plant. The presented thermodynamic cycle is partially similar to a design presented by Jericha [19]. The GRAZ cycle contains a conventional condenser, heat recovery steam generator, series of devices for hierarchic energy conversion, and CO_2 compressor to increase CO_2 share in working fluid. Contrary to the authors design, the GRAZ containing cycle is not compact. The presented cycle allows construction of a power plant which can find more various applications. This is followed by the determination of cycle parameters and the impact of a spray-ejector condenser (SEC) on efficiency and energy conversion enhancement. To state the main point, it has been found that:

1. The use of a spray-ejector condenser leads to an efficiency decrease of approximately 5.91 percentage points, with the simultaneous energy conversion enhancement due to the device's size being reduced by 32 times in the lower heat source area.
2. Furthermore, for the wet combustion chamber to achieve compactness, new cooling design concepts should be developed to bring it into line with the latest transpiration technologies. Additionally, the impact of a wet combustion chamber on the overall operation of the cycle has been estimated, yielding a 30-fold enhancement of energy conversion in the upper heat source area.
3. The total efficiency of the system is $\eta_{el-netto}$ = 37.78%. However, the installation of such a system provides a perspective on meeting the needs of small and large cities to produce heat and electricity with minimal negative—or even a positive—impact on the environment.

It is worth stressing that the presented power plant does not emit carbon dioxide into the atmosphere. Advantages of this power plant concerning greenhouse gases reduction are:

1. The analysed power plant could very well support wind and solar power plants whose energy generation is dependent on weather conditions. Unfortunately, wind and solar power plants are usually supported by conventional gas power plants, which decrease reduction of green-house emissions [151,152].
2. In the laws of many countries, biomass is considered as a carbon-free energy source [153–155]. If the analysed cycle is supplied by biogas, it leads to negative carbon dioxide emission [156]. Furthermore, in this situation carbon dioxide from biomass would be captured and sequestrated.

3. The proposed method of carbon capture utilises only physical processes and does not apply chemical ones, such as amine [157,158]. Because the captured carbon dioxide is pure and does not contain amines, such carbon dioxide is easier to store and sequestrate.

4. It is possible to produce methanol from captured CO_2 thanks to its purity. However, this solution would require additional devices [159,160] which were not pretested in this article.

A power plant which operates on the presented thermal cycle can find various applications. Compact dimensions in comparison to the GRAZ cycle provide opportunities for utilization. A miniaturised version of this power plant can be used for small biogas power plants, because a smaller power plant would be easier to implement for distributed energy sources [161–164]. Maritime applications, such as ships and offshore rigs, are another example of possible places of application. Available space and mass of the power unit are essential for that kind of application.

The focus of further research on the development of transpiration cooling should centre on procedures to facilitate the transition from a solution worked out for a single canal to one covering an entire porous structure with the effect of standardizing equations describing Poiseuille–Knudsen–Reynolds types of flows [75,109]. For such a model, it is possible to significantly slash the number of experiments necessary to find transmittance coefficients, Knudsen diffusion, and Reynolds thermal transpiration.

Nomenclature

A	surface area, m^2
c	velocity in CFD approach, m/s
c	velocity in CFM approach, m/s
D	diffusive stress tensor, Pa
$\dot{E}$	available energy rate, kW
$\mathbf{e}_r$	unit vector in radius direction
$\mathbf{e}_x$	unit vector in axial direction
	$e = u + p/\rho + zg + (c^2)/2$—specific total energy, J/kg
F	force, N
f	forces comes from the surface mechanism, N/m^2

g	gravitation acceleration, m/s^2
h	specific enthalpy, kJ/kg
$\mathbf{I}$	Gibbs unit tensor, -
$\mathbf{n}$	unit vector normal to section
N	power, kW
$\dot{m}$	mass flow rate, kg/s
$\mathbf{P}$	stress tensor associated with external and internal configuration forces, Pa
p	pressure, MPa
R	gas constant, kJ/(kgK)
$\mathbf{R}$	friction force, N
$\mathcal{R}$	Reynolds stress tensor, Pa
$\dot{Q}$	heat transfer rate, kW
$\dot{Q}_{chem}$	chemical energy transfer rate, kW
q	heat flux density, kW/m^3
s	specific etropy, kJ/(kgK)
$\mathbf{t}$	total momentum flux, Pa
T	temperature, °C
u	specific internal energy, kJ/kg
$\mathbf{v}$	velocity vector, m/s
v	specific volume, m^3/kg
V	volume, m^3
$\dot{V}$	volume flow rate, m^3/s
x	vapour quality, -
X	volumetric fraction or mole fraction, -
Y	mass fraction, -
z	height, m
∂V	the contact area of the solid structure with the working medium
0D	zero-dimensional algebraic model of flow based on integral balances of mass, momentum and energy
3D	three-dimensional model based on differential equations, which requires complete geometry of a flow channel
$\otimes$	dyadic multiplicator
D	pitch diameter of the stage, m
H_s	isentropic static enthalpy drop at the stage; $\frac{\text{kJ}}{\text{kg}}$
h	specific enthalpy; $\frac{\text{kJ}}{\text{kg}}$
$\dot{m}$	mass flow rate; $\frac{\text{kg}}{\text{s}}$
m	mobility coefficients
Ma	Mach number
P	power; MW
s	specific entropy; $\frac{\text{kJ}}{\text{kg} * \text{K}}$
T	temperature in centigrade (Celsius scale); °C
v	specific volume; $\frac{\text{m}^3}{\text{kg}}$
V	volume; m^3
w	specific work, kJ/kg
0D	zero-dimensional algebraic model of flow based on integral balances of mass, momentum and energy
3D	three-dimensional model based on differential equations, which requires complete geometry of a flow channel
CFD	Computational Fluid Dynamics, so-called three-dimensional description of unknowns parameters of the power plant devices

	Greek symbols
Δp	pressure drop, MPa
ΔT	the temperature difference in the heat exchanger, K
η	efficiency
ξ	flow losses for changing diameter channel
ν	surface friction coefficients
π	pressure ratio
Π_c	dimensionless compression ratio
Π_s	dimensionless suction ratio
Π_{cav}	dimensionless cavitation ratio
μ	mass flow capacity coefficient
ρ	density, kg/m^3
$\boldsymbol{\tau}$	viscous stress tensor, Pa
τ	narrowing coefficient
φ	velocity coefficient
χ	volumetric entrainment ratio
χ_m	mass entrainment ratio
	Subscripts and superscripts:
air	air
bap	below ambient pressure
C	compressor
c	compression in spray-ejector condenser
cav	cavitation
CC	combustion chamber
CCU	carbon dioxide capture unit
CHE	cooling heat exchanger
d	diffuser
e	effective
ex	exhaust
el	electrical
f	fuel
G	electric generator
g	gaseous
GT	gas turbine
HE	heat exchanger
i	isentropic, ideal
lq	liquid
m	mechanical
M	motor
MC	mixing chamber
n	nozzle
P	pump
s	isentropic
sc	suction chamber
t	technical
t	total
1s, 2s, . . .	isentropic points of process
1, 2, . . .	real points of process
	Abbreviations:
ASU	air separation unit
bap	below ambient pressure
B	boiler
BC	Brayton cycle

C	compressor
CC	combustion chamber
CCS	carbon dioxide capture and storage systems
CCU	carbon capture unit
CES	clean energy systems
CFD	computational fluid dynamics, so-called three-dimensional description of unknown parameters of the power plant devices
CFM	computational flow mechanics, so-called zero-dimensional description of unknown parameters of the power plant apparatus
CHE	cooling heat exchanger
CSE	spray-ejector condenser
DBC	double Brayton cycle
DBCOCC	double Brayton cycle with oxy-combustion and CO_2 capture
EC	energy consumption
G	electric generator
GT	gas turbine
HE	heat exchanger
HPFC	high-pressure fractionating column
HRSG	heat recovery steam generator
HTC	heat transfer coefficient
LHV	low heating value, kJ/kg
lq	liquid
LPFC	low-pressure fractionating column
M	motor
MC	mixing chamber
MS	molecular sieve
P	pump
RHE	regenerative heat exchanger
sat	saturation
S + CHE	condensate-cooler heat exchanger and separator
SHE	subcooler
TIT	turbine inlet temperature
V	valve
WCC	wet combustion chamber
WS	water separator

References

1. Yantovsky, E.; Górski, J.; Shokotov, M. *Zero Emissions Power Cycles*; CRC Press Taylor & Francis Group: Boca Raton, FL, USA, 2009.
2. Kotowicz, J.; Brzęczek, M.; Job, M. The influence of carbon capture and compression unit on the characteristics of ultramodern combined cycle power plant. *Int. J. Glob. Warn.* **2017**, *12*, 164–187. [CrossRef]
3. Ziółkowski, P.; Badur, J. A study of a compact high-efficiency zero-emission power plant with oxy-fuel combustion. In Proceedings of the 32nd International Conference on Efficiency, Cost, Optimization, Simulation and Environmental Impact of Energy Systems ECOS 2019, Wroclaw, Poland, 23–28 June 2019; Stanek, W., Gładysz, P., Werle, S., Adamczyk, W., Eds.; Institute of Thermal Technology, Silesian University of Technology: Gliwice, Poland, 2019; pp. 1557–1568.
4. Pawlak-Kruczek, H.; Arora, A.; Mościcki, K.; Krochmalny, K.; Sharma, S.; Niedzwiecki, L. A transition of a domestic boiler from coal to biomass—Emissions from combustion of raw and torrefied Palm Kernel shells (PKS). *Fuel* **2020**, *263*, 116718. [CrossRef]
5. Ziółkowski, P.; Badur, J.; Pawlak-Kruczek, H.; Nedźwiecki, Ł.; Kowal, M.; Krochmalny, K. A novel concept of negative CO_2 emission power plant, based on combustion the gas from sewage sludge gasification in a gas turbine with spray-ejector condenser. In Proceedings of the XXIV International Symposium on Combustion Processes, Wrocław, Poland, 23–26 September 2019; pp. 103–104.
6. Badur, J.; Lemański, M.; Kowalczyk, T.; Ziółkowski, P.; Kornet, S. Zero-dimensional robust model of an SOFC with internal re-forming for hybrid energy cycles. *Energy* **2018**, *158*, 128–138. [CrossRef]
7. Ziółkowski, P.; Hyrzyński, R.; Lemański, M.D.; Kraszewski, B.; Bykuć, S.; Głuch, S.; Sowiżdżał, A.; Pająk, L.; Wachowicz-Pyzik, A.; Badur, J. Different design aspects of an Organic Rankine Cycle turbine for electricity production using a geothermal binary power plant. *Energy Convers. Manag.* **2021**, *246*, 114672. [CrossRef]

8. Ziółkowski, P. A thermodynamic analysis of a gas-steam turbine incorporating a full model of a spray—Ejector condenser. *Trans. IFFM* **2018**, *139*, 63–96.

9. Ziółkowski, P. A Thermodynamic Analysis of Low Emission Gas-Steam Cycles with Oxy-Combustion. Ph.D. Thesis, Institute Fluid Flow Machinery, Polish Academy of Sciences, Gdańsk, Poland, 2018. (In Polish).

10. Ziółkowski, P.; Madejski, P.; Amiri, M.; Kuś, T.; Stasiak, K.; Subramanian, N.; Pawlak-Kruczek, H.; Badur, J.; Niedźwiecki, Ł.; Mikielewicz, D. Thermodynamic analysis of negative CO_2 emission power plant using Aspen Plus, Aspen Hysys, and Ebsilon software. *Energies* **2021**, *14*, 6304. [CrossRef]

11. Anderson, R.; Viteri, F.; Hollis, R.; Hebbar, M.; Downs, J.; Davies, D.; Harris, M. Application of Existing Turbomachinery for Zero Emissions Oxy-Fuel Power Systems. In Proceedings of the ASME Turbo Expo 2009: Power for Land, Sea, and Air, Orlando, FL, USA, 8–12 June 2009; pp. 469–479. [CrossRef]

12. Chodkiewicz, R.; Porochnicki, J.; Kaczan, B. Steam–Gas Condensing Turbine System for Power and Heat Generation. In Proceedings of the ASME Turbo Expo 2001: Power for Land, Sea, and Air, New Orleans, LA, USA, 4–7 June 2001. [CrossRef]

13. Hollis, R.; Skutley, P.; Ortíz, C.; Varkey, V.; Lepage, D.; Brown, B.; Davies, D.; Harris, M. Oxy-Fuel Turbomachinery Development for Energy Intensive Industrial Applications. In Proceedings of the ASME Turbo Expo 2012: Turbine Technical Conference and Exposition, Copenhagen, Denmark, 11–15 June 2012; pp. 431–439. [CrossRef]

14. Hustad, C.W.; Tronstad, I.; Anderson, R.; Pronske, K.; Veteri, F. Optimization of thermodynamically efficient nominal 40 MW zero emission pilot and demonstration power plant in Norway. In Proceedings of the ASME Turbo Expo 2005: Power for Land, Sea and Air, Reno, NV, USA, 6–9 June 2005; pp. 271–278.

15. Pronske, K.; Trowsdale, L.; Macadam, S.; Viteri, F.; Bevc, F.; Horazak, D. An overview of turbine and combustor develompent for coal-based oxy-syngas systems. In Proceedings of the ASME Turbo Expo 2006: Power for Land, Sea and Air, Barcelona, Spain, 8–11 May 2006.

16. Anderson, R.; Hustad, C.; Skutley, P.; Hollis, R. Oxy-fuel turbo machinery development for energy intensive industrial applications. *Energy Procedia* **2014**, *63*, 511–523. [CrossRef]

17. Marin, O.; Bourhis, Y.; Di Zanno, P.; Viteri, F.; Anderson, R. High Efficiency, Zero Emission Power Generation Based on a High-Temperature Steam Cycle. In Proceedings of the 28th International Technical Conference on Coal Utilization & Fuel Systems, Clearwater, FL, USA, 9–13 March 2003.

18. Ziółkowski, P. Porous structures in aspects of transpirating cooling of oxycombustion chamber walls. *AIP Conf. Proc.* **2019**, *2077*, 020065. [CrossRef]

19. Jericha, H.; Feshaaki. The GRAZ cycle—1500 °C max temperature potential H_2-O_2 fired CO_2 capture with $C4_4$-O_2 firing. In Proceedings of the 1995 ASME Cogen-Turbo Power Conference, Houston, TX, USA, 5–8 June 1995.

20. Sanz, W.; Hustad, C.-W.; Jericha, H. First Generation Graz Cycle Power Plant for Near-Term Deployment. In Proceedings of the ASME Turbo Expo: Turbine Technical Conference and Exposition, Vancouver, BC, Canada, 6–10 June 2011; pp. 969–979. [CrossRef]

21. Miller, A.; Lewandowski, J.; Badyda, K.; Kiryk, S.; Milewski, J.; Hama, J.; Iki, N. Off-Design analysis of the GRAZ cycle performance. In Proceedings of the International Gas Turbine Congress, Tokyo, Japan, 2–7 November 2003.

22. Kotowicz, J.; Job, M. Thermodynamic and economic analysis of a gas turbine combined cycle plant with oxy-combustion. *Arch. Thermodyn.* **2013**, *34*, 215–233. [CrossRef]

23. Madejski, P.; Chmiel, K.; Subramanian, N.; Kuś, T. Methods and techniques for CO_2 capture: Review of potential solutions and applications in modern energy technologies. *Energies* **2022**, *15*, 887. [CrossRef]

24. Kanniche, M.; Gros-Bonnivard, R.; Jaud, P.; Valle-Marcos, J.; Amann, J.M.; Bouallou, C. Pre-combustion, post-combustion and oxy-combustion in thermal power plant for CO_2 capture. *Appl. Therm. Eng.* **2010**, *30*, 53–62. [CrossRef]

25. Yang, H.J.; Kang, D.W.; Ahn, J.H.; Kim, T.S. Evaluation of design performance of the semi-closed oxy-fuel combustion combined cycle. In Proceedings of the ASME Turbo Expo: Power for Land, Sea and Air 2012, Copenhagen, Denmark, 11–15 June 2012.

26. Yantovski, E.; Zvagolsky, K.; Gavrilenko, V. The COOPERATE—Demo power cycle. *Energy Convers Manag.* **1995**, *36*, 861–864. [CrossRef]

27. Mathieu, P.; Nihart, R. Sensitivity analysis of the MATIANT cycle. *Energy Convers. Manag.* **1999**, *40*, 1687–1700. [CrossRef]

28. Feidt, M. *Finite Physical Dimensions Optimal Thermodynamics 1 Fundamentals*; ISTE Press/Elsevier: London, UK, 2017.

29. Staicovici, M. Further research zero CO_2 emission power production: The 'COOLENERG' process. *Energy* **2002**, *27*, 831–844. [CrossRef]

30. Yantovsky, E.; Górski, J.; Smyth, B.; Elshof, J. Zero-emission fuel-fired power plants with ion transport membrane. *Energy* **2004**, *29*, 2077–2088. [CrossRef]

31. Park, S.K.; Kim, T.S.; Sohn, J.L.; Lee, Y.D. An integrated power generation system combining solid oxide fuel cell and oxy-fuel com-bustion for high performance and CO_2 capture. *Appl. Energy* **2011**, *88*, 1187–1196. [CrossRef]

32. Budzianowski, W. An oxy-fuel mass-recirculating process for H_2 production with CO_2 capture by autothermal catalytic ox-yforming of methane. *Int. J. Hydrogen Energy* **2012**, *35*, 7454–7469. [CrossRef]

33. Badur, J.; Lemański, M.; Kowalczyk, T.; Ziółkowski, P.; Kornet, S. Verification of zero-dimensional model of SOFC with internal fuel reforming for complex hybrid energy cycles. *Chem. Process Eng.* **2018**, *39*, 113–128. [CrossRef]

34. Bolland, O.; Kvamsdal, H.M.; Boden, J.C. A Thermodynamic Comparison of Oxy-Fuel Power Cycles Water-Cycle, Graz-Cycle and Matiant-Cycle. 2001. Available online: https://www.semanticscholar.org/paper/A-thermodynamic-comparison-of-the-oxy-fuel-power-Bolland-Kvamsdal/3887db33cefe667646448c253251c5d8683c1b48 (accessed on 30 December 2021).

35. Kvamsdal, H.M.; Jordal, K.; Bolland, O. A quantitative comparison of gas turbine cycles with CO_2 capture. *Energy* **2007**, *32*, 10–24. [CrossRef]

36. Zhang, N.; Lior, N. Two novel oxy-fuel power cycles integrated with natural gas reforming and CO_2 capture. *Energy* **2008**, *33*, 340–351. [CrossRef]

37. Głuch, S.; Ziółkowski, P.; Witanowski, Ł.; Badur, J. Design and computational fluid dynamics analysis of the last stage of inno-vative gas-steam turbine. *Arch. Thermodyn.* **2021**, *42*, 1–24.

38. Gou, C.; Cai, R.; Hong, H. An Advanced Oxy-Fuel Power Cycle with High Efficiency. *Proc. Inst. Mech. Eng. Part A J. Power Energy* **2006**, *220*, 315–325. [CrossRef]

39. Czakiert, T.; Sztekler, K.; Karski, S.; Markiewicz, D.; Nowak, W. Oxy-fuel circulating fluidized bed combustion in a small pi-lot-scale test rig. *Fuel Process. Technol.* **2010**, *91*, 1617–1623. [CrossRef]

40. Liu, C.; Chen, G.; Sipöcz, N.; Assadi, M.; Bai, X. Characteristics of oxy-fuel combustion in gas turbines. *Appl. Energy* **2011**, *89*, 387–394. [CrossRef]

41. Perrin, N.; Dubettier, R.; Lockwood, F.; Court, P.; Tranier, J.-P.; Bourhy-Weber, C.; Devaux, M. Oxycombustion for carbon capture on coal power plants and industrial processes: Advantages, innovative solutions and key projects. *Energy Procedia* **2013**, *37*, 1389–1404. [CrossRef]

42. Perrin, N.; Paufique, C.; Leclerc, M. Latest performances and improvement perspective of oxycombustion for carbon capture on coal power plants. *Energy Procedia* **2014**, *63*, 524–531. [CrossRef]

43. Saanum, I.; DiTaranto, M. Experimental study of oxy-fuel combustion under gas turbine conditions. *Energy Fuels* **2017**, *31*, 4445–4451. [CrossRef]

44. Krishnamurthy, N.; Paul, J.; Blasiak, W. Studies on low-intensity oxy-fuel burner. *Proc. Combust. Inst.* **2009**, *32*, 3139–3146. [CrossRef]

45. Adamczyk, W.P.; Bialecki, R.A.; Ditaranto, M.; Gladysz, P.; Haugen, N.E.L.; Katelbach-Wozniak, A.; Klimanek, A.; Sladek, S.; Szlek, A.; Wecel, G. CFD modeling and thermodynamic analysis of a concept of a MILD-OXY combustion large scale pulverized coal boiler. *Energy* **2017**, *140*, 1305–1315. [CrossRef]

46. Hjärtstam, S.; Johansson, R.; Andersson, K.; Johnsson, F. Computational fluid dynamics modeling of oxy-fuel flames: The role of soot and gas radiation. *Energy Fuels* **2012**, *26*, 2786–2797. [CrossRef]

47. Ghadamgahi, M.; Ölund, P.; Ekman, T.; Andersson, N.; Jönsson, P. A Comparative CFD study on simulating flameless oxy-fuel combustion in a pilot-scale furnace. *J. Combust.* **2016**, *2016*, 6735971. [CrossRef]

48. Ghadamgahi, M.; Ölund, P.; Lugnet, A.; Pour, M.S.; Yang, W. Design optimization of flameless-oxyfuel soaking pit furnace using CFD technique. *Energy Procedia* **2014**, *61*, 611–614. [CrossRef]

49. Yin, C.; Rosendahl, L.A.; Kær, S.K. Chemistry and radiation in oxy-fuel combustion: A computational fluid dynamics modeling study. *Fuel* **2011**, *90*, 2519–2529. [CrossRef]

50. Lewandowski, M.T.; Ertesvåg, I.S. Analysis of the eddy dissipation concept formulation for MILD combustion modelling. *Fuel* **2018**, *224*, 687–700. [CrossRef]

51. Gładysz, P.; Stanek, W.; Czarnowska, L.; Sładek, S.; Szlęk, A. Thermo-ecological evaluation of an integrated MILD oxy-fuel combustion power plant with CO_2 capture, utilisation, and storage—A case study in Poland. *Energy* **2018**, *144*, 379–392. [CrossRef]

52. Gładysz, P.; Stanek, W.; Czarnowska, L.; Węcel, G.; Langørgen, Ø. Thermodynamic assessment of an integrated MILD oxyfuel combustion power plant. *Energy* **2017**, *137*, 761–774. [CrossRef]

53. Ertesvåg, I.S.; Kvamsdal, H.M.; Bolland, O. Exergy analysis of a gas-turbine combined-cycle power plant with precombustion CO_2 capture. *Energy* **2005**, *30*, 5–39. [CrossRef]

54. Voldsund, M.; Gardarsdottir, S.O.; De Lena, E.; Pérez-Calvo, J.-F.; Jamali, A.; Berstad, D.; Fu, C.; Romano, M.; Roussanaly, S.; Anantharaman, R.; et al. Comparison of technologies for CO_2 capture from cement production—Part 1: Technical evaluation. *Energies* **2019**, *12*, 559. [CrossRef]

55. Skorek-Osikowska, A.; Bartela, Ł.; Kotowicz, J. Economical and ecological evaluation of the advanced electricity production technologies adapter for carbon dioxide capture. *J. Energy Sci.* **2010**, *1*, 147–160.

56. Bartela, Ł.; Skorek-Osikowska, A.; Kotowicz, J. Thermodynamic, ecological and economic aspects of the use of the gas turbine for heat supply to the stripping process in a supercritical CHP plant integrated with a carbon capture installation. *Energy Convers. Manag.* **2014**, *85*, 750–763. [CrossRef]

57. Tlili, N.; Grévillot, G.; Vallières, C. Carbon dioxide capture and recovery by means of TSA and/or VSA. *Int. J. Greenh. Gas Control* **2009**, *3*, 519–527. [CrossRef]

58. Asendrych, D.; Niegodajew, P. Numerical Study of the CO_2 Absorber Performance Subjected to the Varying Amine Solvent and Flue Gas Loads. *Chem. Eng. Commun.* **2016**, *204*, 580–590. [CrossRef]

59. Abu Zahra, M.; Schneiders, L.H.; Niederer, J.P.; Feron, P.H.; Versteeg, G.F. CO_2 capture from power plants: Part I. A parametric study of the technical performance based on monoethanolamine. *Int. J. Greenh. Gas Control* **2007**, *1*, 37–46. [CrossRef]

60. Ziółkowski, P.; Lemański, M.; Badur, J.; Nastałek, L. Power augmentation of PGE Gorzów gas turbine by steam injection—Thermodynamic overview. *Rynek Energii* **2012**, *98*, 161–167.

61. Cheng, D.Y. The distinction between Cheng and STIG cycle. In Proceedings of the ASME Turbo Expo 2006: Power for Land, Sea, and Air, Barcelona, Spain, 8–11 May 2006.

62. Normann, F.; Andersson, K.; Leckner, B.; Johnsson, F. Emission control of nitrogen oxides in the oxy-fuel process. *Prog. Energy Combust. Sci.* **2009**, *35*, 385–397. [CrossRef]

63. Wang, Y.; Huang, Y.; McIlveen-Wright, D.; McMullan, J.; Hewitt, N.; Eames, P.; Rezvani, S. A techno-economic analysis of the ap-plication of continuous stage-combustion and flameless oxidation to the combustor design in gas turbines. *Fuel Process. Technol.* **2006**, *87*, 727–736. [CrossRef]

64. Wienchol, P.; Szlęk, A.; Ditaranto, M. Waste-to-energy technology integrated with carbon capture—Challenges and opportuni-ties. *Energy* **2020**, *198*, 117352. [CrossRef]

65. Binnion, M. How the technical differences between shale gas and conventional gas projects lead to a new business model be-ing required to be successful. *Mar. Pet. Geol.* **2012**, *31*, 3–7. [CrossRef]

66. Gabicz, M.; Sokół, H. Polish natural gas market after the arrival of the fiasco with shale deposits in Poland. *Rynek Energii* **2015**, *121*, 3–7. (In Polish)

67. Kinnaman, T.C. The economic impact of shale gas extraction: A review of existing studies. *Ecol. Econ.* **2011**, *70*, 1243–1249. [CrossRef]

68. Rahm, D. Regulating hydraulic fracturing in shale gas plays: The case of Texas. *Energy Policy* **2011**, *39*, 2974–2981. [CrossRef]

69. Jenner, S.; Lamadrid, A.J. Shale gas vs. coal: Policy implications from environmental impact comparisons of shale gas, conventional gas, and coal on air, water, and land in the United States. *Energy Policy* **2013**, *53*, 442–453. [CrossRef]

70. Mendecka, B.; Lombardi, L.; Gladysz, P. Waste to energy efficiency improvements: Integration with solar thermal energy. *Waste Manag. Res. J. Sustain. Circ. Econ.* **2019**, *37*, 419–434. [CrossRef]

71. Pawlak-Kruczek, H.; Wnukowski, M.; Niedzwiecki, L.; Czerep, M.; Kowal, M.; Krochmalny, K.; Zgóra, J.; Ostrycharczyk, M.; Baranowski, M.; Tic, W.J.; et al. Torrefaction as a valorization method used prior to the gasification of sewage sludge. *Energies* **2019**, *12*, 175. [CrossRef]

72. Pawlak-Kruczek, H.; Wnukowski, M.; Niedzwiecki, L.; Kowal, M.; Krochmalny, K. Gasification of torrefied sewage sludge with the addition of calcium carbonate. *J. Energy Resour. Technol.* **2020**, *142*, 070910. [CrossRef]

73. Ziółkowski, P.; Kowalczyk, T.; Lemański, M.; Badur, J. On energy, exergy, and environmental aspects of a combined gas-steam cycle for heat and power generation undergoing a process of retrofitting by steam injection. *Energy Convers. Manag.* **2019**, *192*, 374–384. [CrossRef]

74. Ziółkowski, P.; Badur, J.; Ziółkowski, P.J. An energetic analysis of a gas turbine with regenerative heating using turbine extrac-tion at intermediate pressure—Brayton cycle advanced according to Szewalski's idea. *Energy* **2019**, *185*, 76–86. [CrossRef]

75. Ziółkowski, P.; Badur, J. On Navier slip and Reynolds transpiration numbers. *Arch. Mech.* **2018**, *70*, 269–300.

76. Smith, A.; Klosek, J. A review of air separation technologies and their integration with energy conversion processes. *Fuel Process. Technol.* **2001**, *70*, 115–134. [CrossRef]

77. Burdyny, T.; Struchtrup, H. Hybrid membrane/cryogenic separation of oxygen from air for use in the oxy-fuel process. *Energy* **2010**, *35*, 1884–1897. [CrossRef]

78. Darde, A.; Prabhakar, R.; Tranier, J.-P.; Perrin, N. Air separation and flue gas compression and purification units for oxy-coal combustion systems. *Energy Procedia* **2009**, *1*, 527–534. [CrossRef]

79. Banaszkiewicz, T.; Chorowski, M.; Gizicki, W. Comparative Analysis of Oxygen Production for Oxy-combustion Application. *Energy Procedia* **2014**, *51*, 127–134. [CrossRef]

80. Van Der Ham, L.V.; Kjelstrup, S. Exergy analysis of two cryogenic air separation processes. *Energy* **2010**, *35*, 4731–4739. [CrossRef]

81. Zhu, Y.; Legg, S.; Laird, C.D. Optimal design of cryogenic air separation columns under uncertainty. *Comput. Chem. Eng.* **2010**, *34*, 1377–1384. [CrossRef]

82. Fu, Q.; Kansha, Y.; Song, C.; Liu, Y.; Ishizuka, M.; Tsutsumi, A. An elevated-pressure cryogenic air separation unit based on self-heat recuperation technology for integrated gasification combined cycle systems. *Energy* **2016**, *103*, 440–446. [CrossRef]

83. Tesch, S.; Morosuk, T.; Tsatsaronis, G. Advanced exergy analysis applied to the process of regasification of LNG (liquefied natu-ral gas) integrated into an air separation process. *Energy* **2016**, *117*, 550–561. [CrossRef]

84. Mehrpooya, M.; Zonouz, M.J. Analysis of an integrated cryogenic air separation unit, oxy-combustion carbon dioxide power cycle and liquefied natural gas regasification process by exergoeconomic method. *Energy Convers. Manag.* **2017**, *139*, 245–259. [CrossRef]

85. Aneke, M.; Wang, M. Process analysis of pressurized oxy-coal power cycle for carbon capture application integrated with liq-uid air power generation and binary cycle engines. *Appl. Energy* **2015**, *154*, 556–566. [CrossRef]

86. Hanak, D.P.; Powell, D.; Manovic, V. Techno-economic analysis of oxy-combustion coal-fired power plant with cryogenic oxy-gen storage. *Appl. Energy* **2017**, *191*, 193–203. [CrossRef]

87. Fu, C.; Vikse, M.; Gundersen, T. Work and heat integration: An emerging research area. *Energy* **2018**, *158*, 796–806. [CrossRef]

88. Yu, H.; Fu, C.; Gundersen, T. Work Exchange Networks (WENs) and Work and Heat Exchange Networks (WHENs): A Review of the Current State of the Art. *Ind. Eng. Chem. Res.* **2019**, *59*, 507–525. [CrossRef]

89. Blaise, M.; Feidt, M.; Maillet, D. Influence of the working fluid properties on optimized power of an irreversible finite dimensions Carnot engine. *Energy Convers. Manag.* **2018**, *163*, 444–456. [CrossRef]

90. Badur, J.; Kowalczyk, T.; Ziółkowski, P.; Tokarczyk, P.; Woźniak, M. Study of the effectiveness of the turbine condenser air extraction system using hydro ejectors. *Trans IFFM* **2016**, *131*, 41–53.

91. Marto, P.J.; Nunn, R.H. *Power Condenser Heat Transfer Technology: Computer modelling/Design/Fouling*; Hemisphere Publishing Corporation: Washington, DC, USA, 1981.

92. Strušnik, D.; Golob, M.; Avsec, J. Effect of non-condensable gas on heat transfer in steam turbine condenser and modelling of ejector pump system by controlling the gas extraction rate through extraction tubes. *Energy Convers. Manag.* **2016**, *126*, 228–246. [CrossRef]

93. Trela, M.; Kwidzinski, R.; Butrymowicz, D.; Karwacki, J. Exergy analysis of two-phase steam–water injector. *Appl. Therm. Eng.* **2010**, *30*, 340–346. [CrossRef]

94. Goliński, J.; Troskaliński, A. *Ejectors Theory and Design (Strumienice Teoria i Konstrukcja)*; WNT: Warsaw, Poland, 1979. (In Polish)

95. Neve, R. Diffuser performance in two-phase jet pumps. *Int. J. Multiph. Flow* **1991**, *17*, 267–272. [CrossRef]

96. Banasiak, K.; Hafner, A. 1D Computational model of a two-phase R744 ejector for expansion work recovery. *Int. J. Therm. Sci.* **2011**, *50*, 2235–2247. [CrossRef]

97. Śmierciew, K.; Butrymowicz, D.; Kwidziński, R.; Przybyliński, T. Analysis of application of two-phase injector in ejector refriger-ation systems for isobutane. *Appl. Therm. Eng.* **2015**, *78*, 630–639. [CrossRef]

98. He, S.; Li, Y.; Wang, R.Z. Progress of mathematical modelling on ejectors. *Renew. Sustain. Energy Rev.* **2009**, *13*, 1760–1780. [CrossRef]

99. Yuan, G.; Zhang, L.; Zhang, H.; Wang, Z. Numerical and experimental investigation of performance of the liquid–gas and liquid jet pumps in desalination systems. *Desalination* **2011**, *276*, 89–95. [CrossRef]

100. Banasiak, K.; Palacz, M.; Hafner, A.; Buliński, Z.; Smołka, J.; Nowak, A.J.; Fic, A. A CFD-based investigation of the energy perfor-mance of two-phase R744 ejectors to recover the expansion work in refrigeration systems: An irreversibility analysis. *Int. J. Refrig.* **2014**, *40*, 328–337. [CrossRef]

101. Sag, N.B.; Ersoy, H.K.; Hepbasli, A.; Halkaci, H. Energetic and exergetic comparison of basic and ejector expander refrigeration systems operating under the same external conditions and cooling capacities. *Energy Convers. Manag.* **2015**, *90*, 184–194. [CrossRef]

102. Colarossi, M.; Trask, N.; Schmidt, D.P.; Bergander, M.J. Multidimensional modeling of condensing two-phase ejector flow. *Int. J. Refrig.* **2012**, *35*, 290–299. [CrossRef]

103. Ameur, K.; Aidoun, Z.; Ouzzane, M. Modeling and numerical approach for the design and operation of two-phase ejectors. *Appl. Therm. Eng.* **2016**, *109*, 809–818. [CrossRef]

104. Witte, J.H. Mixing Shocks and Their Influence on the Design of Liquid-Gas Ejectors. Ph.D. Thesis, Uitgeverij Waltman, TU Delft, The Netherlands, 1962.

105. Witte, J.H. Mixing shocks in two-phase flow. *J. Fluid Mech.* **1969**, *36*, 639–655. [CrossRef]

106. Biswas, M.N.; Mitra, A.K. Momentum transfer in horizontal multi-jet liquid-gas ejector. *Can. J. Chem. Eng.* **1981**, *59*, 634–637. [CrossRef]

107. Cunningham, R.G. Gas Compression with the Liquid Jet Pump. *J. Fluids Eng.* **1974**, *96*, 203–215. [CrossRef]

108. Cunningham, R.G.; Hansen, A.G.; Na, T.Y. Jet pump cavitation. *J. Fluids Eng.* **1970**, *3*, 483–494. [CrossRef]

109. Ziółkowski, P.; Badur, J. A theoretical, numerical and experimental verification of the Reynolds thermal transpiration law. *Int. J. Numer. Methods Heat Fluid Flow* **2018**, *28*, 64–80. [CrossRef]

110. Badur, J.; Banaszkiewicz, M. Model of the ideal fluid with scalar microstructure. An application to flashing flow of water. *Trans. IFFM* **1999**, *105*, 115–152.

111. Bilicki, Z.; Badur, J. A thermodynamically consistent relaxation model for a turbulent, binary mixture undergoing phase transi-tion. *J. Non-Equilib. Thermodyn.* **2003**, *28*, 145–172. [CrossRef]

112. Sharma, V.P.; Kumaraswamy, S.; Mani, A. Effect of various nozzle profiles on performance of a two phase flow jet pump. *World Acad. Sci. Eng. Technol.* **2012**, *6*, 173–179.

113. Havelka, P.; Linek, V.; Sinkule, J.; Zahradník, J.; Fialova, M. Effect of the ejector configuration on the gas suction rate and gas hold-up in ejector loop reactors. *Chem. Eng. Sci.* **1997**, *52*, 1701–1713. [CrossRef]

114. Elbel, S. Historical and present developments of ejector refrigeration systems with emphasis on transcritical carbon dioxide air-conditioning applications. *Int. J. Refrig.* **2011**, *34*, 1545–1561. [CrossRef]

115. Biń, A.K. Gas entrainment by plunging liquid jets. *Chem. Eng. Sci.* **1993**, *48*, 3585–3630. [CrossRef]

116. Ziółkowski, P.; Badur, J. Navier number and transition to turbulence. *J. Phys. Conf. Ser.* **2014**, *530*, 012035. [CrossRef]

117. Badur, J.; Ziółkowski, P.; Zakrzewski, W.; Sławiński, D.; Banaszkiewicz, M.; Kaczmarczyk, O.; Kornet, S.; Ziółkowski, P.J. On the surface vis impressa caused by a fluid-solid contact. In *Shell Structure Theory and Applications*; Pietraszkiewicz, W., Górski, J., Eds.; Taylor & Francis: London, UK, 2014; Volume 3, pp. 53–56.

118. Badur, J.; Ziółkowski, P.J.; Ziółkowski, P. On the angular velocity slip in nano flows. *Microfluid. Nanofluid.* **2015**, *19*, 191–198. [CrossRef]

119. Badur, J.; Ziółkowski, P.; Zakrzewski, W.; Sławiński, D.; Kornet, S.; Kowalczyk, T.; Hernet, J.; Piotrowski, R.; Felincjancik, J. An advanced Thermal-FSI approach to flow heating/cooling. *J. Phys. Conf. Ser.* **2014**, *530*, 012039. [CrossRef]

120. Badur, J.; Ziółkowski, P.; Kornet, S.; Kowalczyk, T.; Banaś, K.; Bryk, M.; Ziółkowski, P.J.; Stajnke, M. Enhanced energy conversion as a result of fluid-solid interaction in micro- and nanoscale. *J. Theor. Appl. Mech.* **2018**, *56*, 329–332. [CrossRef]

121. Butterworth, M.; Sheer, T. High-pressure water as the driving fluid in an ejector refrigeration system. *Appl. Therm. Eng.* **2007**, *27*, 2145–2152. [CrossRef]

122. Kowalczyk, T.; Głuch, J.; Ziółkowski, P. Analysis of Possible Application of High-Temperature Nuclear Reactors to Contemporary Large-Output Steam Power Plants on Ships. *Pol. Marit. Res.* **2016**, *23*, 32–41. [CrossRef]

123. Lemański, M.; Karcz, M. Performance of lignite-syngas operated tubular Solid Oxide Fuell Cell. *Chem. Process. Eng.* **2008**, *29*, 233–248.

124. Szewczuk-Krypa, N.; Drosińska-Komor, M.; Głuch, J.; Breńkacz, Ł. Comparison analysis of selected nuclear power plants supplied with helium from high-temperature gas-cooled reactor. *Pol. Marit. Res.* **2018**, *25*, 204–210. [CrossRef]

125. Martinaitis, V.; Rimdžius, D.; Bielskus, J.; Streckienė, G.; Motuzienė, V. Preliminary comparison of the performance of thermodynamic models of the subsonic ejector and turbofan. *J. Mech. Eng.* **2020**, *66*, 325–336. [CrossRef]

126. Kowalczyk, T.; Badur, J.; Ziółkowski, P. Comparative study of a bottoming SRC and ORC for Joule–Brayton cycle cooling modular HTR exergy losses, fluid-flow machinery main dimensions, and partial loads. *Energy* **2020**, *206*, 118072. [CrossRef]

127. Ziółkowski, P.; Kowalczyk, T.; Kornet, S.; Badur, J. On low-grade waste heat utilization from a supercritical steam power plant using an ORC-bottoming cycle coupled with two sources of heat. *Energy Convers. Manag.* **2017**, *146*, 158–173. [CrossRef]

128. Kowalczyk, T.; Ziółkowski, P.; Badur, J. Exergy Losses in the Szewalski Binary Vapor Cycle. *Entropy* **2015**, *17*, 7242–7265. [CrossRef]

129. Ziółkowski, P.; Zakrzewski, W.; Kaczmarczyk, O.; Badur, J. Thermodynamic analysis of the double Brayton cycle with the use of oxy combustion and capture of CO_2. *Arch. Thermodyn.* **2013**, *34*, 23–38. [CrossRef]

130. Topolski, J.; Badur, J. Comparison of the combined cycle efficiencies with different heat recovery steam generators. *Trans. IFFM* **2002**, *111*, 5–16.

131. Chmielniak, T.; Trela, M. *Diagnostics of New-Generation Thermal Power Plants*; IMP PAN Publisher: Gdańsk, Poland, 2008.

132. Tindell, R.H.; Alston, T.M.; Sarro, C.A.; Stegmann, G.C.; Gray, L.; Davids, J. Computational Fluid Dynamics Analysis of a Steam Power Plant Low-Pressure Turbine Downward Exhaust Hood. *J. Eng. Gas Turbines Power* **1996**, *118*, 214–224. [CrossRef]

133. Veerabathraswamy, K.; Kumar, A.S. Effective boundary conditions and turbulence modeling for the analysis of steam turbine exhaust hood. *Appl. Therm. Eng.* **2016**, *103*, 773–780. [CrossRef]

134. Śmierciew, K.; Butrymowicz, D.; Przybyliński, T.; Pawluczuk, A. Investigations of heat and momentum transfer in two-phase injector operating with isobutene. *Appl. Therm. Eng.* **2017**, *127*, 1495–1505. [CrossRef]

135. Burton, Z.; Ingram, G.L.; Hogg, S. A literature review of low pressure steam turbine exhaust hood and diffuser studies. *J. Eng. Gas Turbines Power* **2013**, *135*, 062001. [CrossRef]

136. Szulc, O.; Doerffer, P.; Tejero, F. Passive control of rotorcraft high-speed impulsive noise. *J. Phys. Conf. Ser.* **2016**, *760*, 012031. [CrossRef]

137. Ochrymiuk, T. Numerical prediction of film cooling effectiveness over flat plate using variable turbulent Prandtl number clo-sures. *J. Therm. Sci.* **2016**, *25*, 280–286. [CrossRef]

138. Ziółkowski, P.; Witanowski, Ł.; Klonowicz, P.; Głuch, S. Optimizationof the last stage of gas-steam turbine using a hybrid method. In Proceedings of the 14th European Conference on Turbomachinery Fluid Dynamics and Thermodynamics ETC 2021, Gdansk, Poland, 12–16 April 2021.

139. Ziółkowski, P.; Głuch, S.; Kowalczyk, T.; Badur, J. Revalorisation of the Szewalski's concept of the law of varying the last-stage blade retraction in a gas-steam turbine. *E3S Web Conf.* **2021**, *323*, 34. [CrossRef]

140. Witanowski, Ł.; Klonowicz, P.; Lampart, P.; Suchocki, T.; Jędrzejewski, Ł.; Zaniewski, D.; Klimaszewski, P. Optimization of an axial turbine for a small scale ORC waste heat recovery system. *Energy* **2020**, *205*, 118059. [CrossRef]

141. Klonowicz, P.; Witanowski, Ł.; Suchocki, T.; Jędrzejewski, Ł.; Lampart, P. Selection of optimum degree of partial admission in a laboratory organic vapour microturbine. *Energ. Convers. Manag.* **2019**, *202*, 112189. [CrossRef]

142. Lampart, P.; Witanowski, Ł.; Klonowicz, P. Efficiency Optimisation of Blade Shape in Steam and ORC Turbines. *Mech. Mech. Eng.* **2018**, *22*, 553–564. [CrossRef]

143. Madejski, P.; Taler, D. Analysis of temperature and stress distribution of superheater tubes after attemperation or sootblower activation. *Energy Convers. Manag.* **2013**, *71*, 131–137. [CrossRef]

144. Badur, J.; Ziółkowski, P.; Sławiński, D.; Kornet, S. An approach for estimation of water wall degradation within pulverized-coal boilers. *Energy* **2015**, *92*, 142–152. [CrossRef]

145. Kantorek, M.; Jesionek, K.; Polesek-Karczewska, S.; Ziółkowski, P.; Badur, J. Thermal utilization of meat and bone meals. Performance analysis in terms of drying process, pyrolysis and kinetics of volatiles combustion. *Fuel* **2019**, *254*, 115548. [CrossRef]

146. Rybiński, W.; Mikielewicz, J. Analytical 1D models of the wall thermal resistance of rectangular minichannels applied in heat exchangers. *Arch. Thermodyn.* **2016**, *37*, 63–78. [CrossRef]

147. Ziółkowski, P.; Szewczuk-Krypa, N.; Butterweck, A.; Stjanke, M.; Głuch, S.; Drosińska-Komor, M.; Milewska, A.; Głuch, J. Comprehensive thermodynamic analysis of steam storage in a steam cycle in a different regime of work: A zero-dimensional and three-dimensional approach. *J. Energy Resour. Technol. Trans. ASME* **2021**, *143*, 050905. [CrossRef]

148. Perycz, S. *Steam and Gas Turbines*; Wydawnictwo Politechniki Gdańskiej: Gdańsk, Poland, 1988. (In Polish)

149. Jaremkiewicz, M.; Dzierwa, P.; Taler, D.; Taler, J. Monitoring of transient thermal stresses in pressure components of steam boilers using an innovative technique for measuring the fluid temperature. *Energy* **2019**, *175*, 139–150. [CrossRef]

150. Jaremkiewicz, M.; Taler, D.; Dzierwa, P.; Taler, J. Determination of transient fluid temperature and thermal stresses in pressure thick-walled elements using a new design thermometer. *Energies* **2019**, *12*, 222. [CrossRef]

151. Hyrzyński, R.; Ziółkowski, P.; Gotzman, S.; Kraszewski, B.; Ochrymiuk, T.; Badur, J. Comprehensive thermodynamic analysis of the CAES system coupled with the underground thermal energy storage taking into account global, central and local level of energy conversion. *Renew. Energy* **2021**, *169*, 379–403. [CrossRef]

152. Rayati, M.; Goodarzi, H.; Ranjbar, A. Optimal bidding strategy of coordinated wind power and gas turbine units in real-time market using conditional value at risk. *Int. Trans. Electr. Energy Syst.* **2018**, *29*, e2645. [CrossRef]

153. Vishwajeet; Pawlak-Kruczek, H.; Baranowski, M.; Czerep, M.; Chorążyczewski, A.; Krochmalny, K.; Ostrycharczyk, M.; Ziółkowski, P.; Madejski, P.; Mączka, T.; et al. Entrained Flow Plasma Gasification of Sewage Sludge–Proof-of-Concept and Fate of Inorganics. *Energies* **2022**, *15*, 1948. [CrossRef]

154. Abam, F.; Diemuodeke, O.; Ekwe, E.; Alghassab, M.; Samuel, O.; Khan, Z.; Imran, M.; Farooq, M. Exergoeconomic and Environmental Modeling of Integrated Polygeneration Power Plant with Biomass-Based Syngas Supplemental Firing. *Energies* **2020**, *13*, 6018. [CrossRef]

155. Kantorek, M.; Jesionek, K.; Polesek-Karczewska, S.; Ziółkowski, P.; Stajnke, M.; Badur, J. Thermal utilization of meat-and-bone meal using the rotary kiln pyrolyzer and the fluidized bed boiler—The performance of pilot-scale installation. *Renew. Energy* **2020**, *164*, 1447–1456. [CrossRef]

156. Ziółkowski, P.; Badur, J.; Kruczek, H.P.; Stasiak, K.; Amiri, M.; Niedzwiecki, L.; Krochmalny, K.; Mularski, J.; Madejski, P.; Mikielewicz, D. Mathematical modelling of gasification process of sewage sludge in reactor of negative CO_2 emission power plant. *Energy* **2021**, *244*, 122601. [CrossRef]

157. Ünveren, E.E.; Monkul, B.O.; Sarıoğlan, S.; Karademir, N.; Alper, E. Solid amine sorbents for CO_2 capture by chemical adsorption: A review. *Petroleum* **2017**, *3*, 37–50. [CrossRef]

158. Li, H.; Yan, J.; Campana, P.E. Feasibility of integrating solar energy into a power plant with amine-based chemical absorption for CO_2 capture. *Int. J. Greenh. Gas Control* **2012**, *9*, 272–280. [CrossRef]

159. Atsonios, K.; Panopoulos, K.D.; Kakaras, E. Investigation of technical and economic aspects for methanol production through CO_2 hydrogenation. *Int. J. Hydrogen Energy* **2016**, *41*, 2202–2214. [CrossRef]

160. Bowker, M. Methanol Synthesis from CO_2 Hydrogenation. *ChemCatChem* **2019**, *11*, 4238–4246. [CrossRef]

161. Aigba, P.A.; Emovon, I.; Samuel, O.D.; Chintua, E.C.; Abdeljawad, T.; Al-Mdallal, Q.M.; Afzal, A. Exergetic Assessment of Waste Gas to Energy in a Novel Integrated NGL Recovery and Power Generation Plant. *Front. Energy Res.* **2022**, *9*, 798896. [CrossRef]

162. Giwa, S.O.; Nwaokocha, C.N.; Samuel, D.O. Off-grid gasoline-powered generators: Pollutants' footprints and health risk assessment in Nigeria. *Energy Sour. Part A: Recover. Util. Environ. Eff.* **2019**, 1–18. [CrossRef]

163. Okwu, M.O.; Samuel, O.D.; Ewim, D.R.E.; Huan, Z. Estimation of biogas yields produced from combination of waste by implementing response surface methodology (RSM) and adaptive neuro-fuzzy inference system (ANFIS). *Int. J. Energy Environ. Eng.* **2021**, *12*, 353–363. [CrossRef]

164. Okwu, M.O.; Tartibu, L.K.; Samuel, O.D.; Omoregbee, H.O.; Ivbanikaro, A.E. Predictive Ability of Response Surface Methodology (RSM) and Artificial Neural Network (ANN) to Approximate Biogas Yield in a Modular Biodigester. *Int. Work-Conf. Artif. Neural Netw.* **2021**, *12861*, 202–215. [CrossRef]